Article

Neuron

The Autism-Associated Gene *Scn2a* Contributes to Dendritic Excitability and Synaptic Function in the Prefrontal Cortex

Graphical Abstract

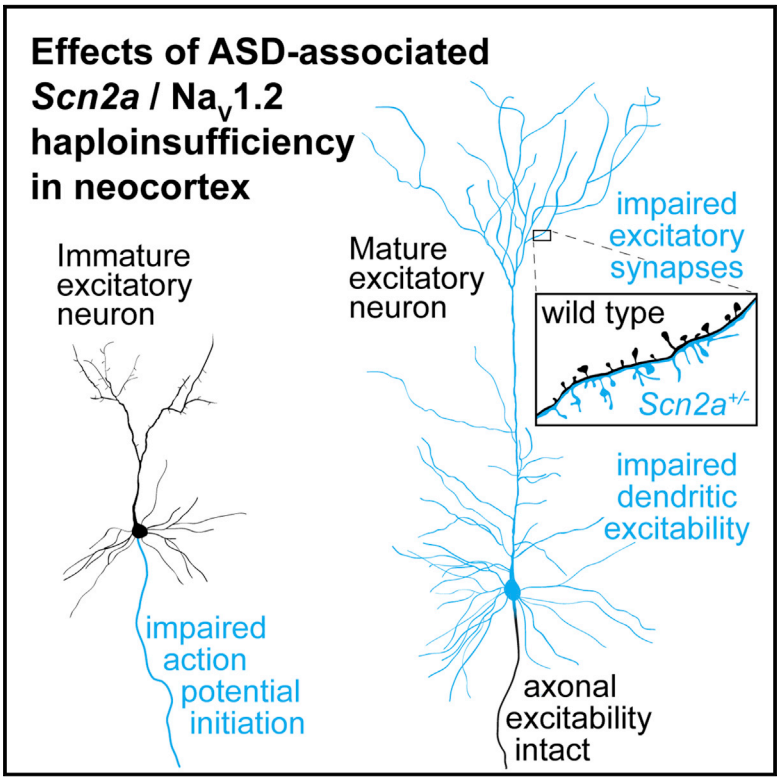

Highlights

- Protein truncation in *SCN2A*/Na$_V$1.2 bears considerable autism spectrum disorder risk
- Na$_V$1.2 governs action potential initiation in immature neocortical pyramidal cells
- Mature *Scn2a*$^{+/-}$ neurons have impaired dendritic excitability and excitatory synapses
- Cell-autonomous loss of Na$_V$1.2 in mature cells alone impairs synaptic function

Authors

Perry W.E. Spratt, Roy Ben-Shalom, Caroline M. Keeshen, Kenneth J. Burke, Jr., Rebecca L. Clarkson, Stephan J. Sanders, Kevin J. Bender

Correspondence

kevin.bender@ucsf.edu

In Brief

Haploinsufficiency in the gene *SCN2A*, which encodes the sodium channel Na$_V$1.2, has strong autism association. Spratt et al. show that *Scn2a* contributes to dendritic excitability in mature neocortical pyramidal cells, where its loss impairs excitatory synaptic function and plasticity.

Spratt et al., 2019, Neuron *103*, 1–13
August 21, 2019
https://doi.org/10.1016/j.neuron.2019.05.037

CellPress

Please cite this article in press as: Spratt et al., The Autism-Associated Gene *Scn2a* Contributes to Dendritic Excitability and Synaptic Function in the Prefrontal Cortex, Neuron (2019), https://doi.org/10.1016/j.neuron.2019.05.037

Neuron
Article

The Autism-Associated Gene *Scn2a* Contributes to Dendritic Excitability and Synaptic Function in the Prefrontal Cortex

Perry W.E. Spratt,[1,2,4] Roy Ben-Shalom,[1,2,4] Caroline M. Keeshen,[1,2] Kenneth J. Burke, Jr.,[1,2] Rebecca L. Clarkson,[1,2] Stephan J. Sanders,[1,3] and Kevin J. Bender[1,2,5,*]
[1]Weill Institute for Neurosciences, University of California, San Francisco, San Francisco, CA, USA
[2]Department of Neurology, University of California, San Francisco, San Francisco, CA, USA
[3]Department of Psychiatry, University of California, San Francisco, San Francisco, CA, USA
[4]These authors contributed equally
[5]Lead Contact
*Correspondence: kevin.bender@ucsf.edu
https://doi.org/10.1016/j.neuron.2019.05.037

SUMMARY

Autism spectrum disorder (ASD) is strongly associated with *de novo* gene mutations. One of the most commonly affected genes is *SCN2A*. ASD-associated *SCN2A* mutations impair the encoded protein $Na_V1.2$, a sodium channel important for action potential initiation and propagation in developing excitatory cortical neurons. The link between an axonal sodium channel and ASD, a disorder typically attributed to synaptic or transcriptional dysfunction, is unclear. Here we show that $Na_V1.2$ is unexpectedly critical for dendritic excitability and synaptic function in mature pyramidal neurons in addition to regulating early developmental axonal excitability. $Na_V1.2$ loss reduced action potential backpropagation into dendrites, impairing synaptic plasticity and synaptic strength, even when $Na_V1.2$ expression was disrupted in a cell-autonomous fashion late in development. These results reveal a novel dendritic function for $Na_V1.2$, providing insight into cellular mechanisms probably underlying circuit and behavioral dysfunction in ASD.

INTRODUCTION

High-throughput sequencing has implicated numerous genes in autism spectrum disorder (ASD) (Sanders et al., 2015). These genes cluster into two groups: chromatin modifiers and genes that support synaptic function (De Rubeis et al., 2014; Sanders et al., 2015). Surprisingly, *SCN2A*, the gene with the most robust ASD association (Ben-Shalom et al., 2017; Sanders et al., 2012; Satterstrom et al., 2018), does not readily fit within either group. *SCN2A* encodes the protein $Na_V1.2$, a voltage-gated sodium channel known to be expressed in the axon initial segment (AIS), an axonal subcompartment adjacent to the soma that is the site of action potential (AP) initiation (Bender and Trussell, 2012; Kole and Stuart, 2012). Interestingly, *SCN2A* variants with different effects on channel function are associated with distinct neurodevelopmental disorders. Heterozygous loss-of-function variants (haploinsufficiency) in *SCN2A* that diminish or eliminate channel function are strongly associated with ASD as well as intellectual disability (ID), whereas gain-of-function missense variants are strongly associated with infantile epilepsy of varying severity (Begemann et al., 2019; Ben-Shalom et al., 2017; Sanders et al., 2018; Wolff et al., 2017). Although neuronal hyperexcitability because of gain-of-function *SCN2A* variants likely contributes to infantile epilepsy, the neuropathological mechanisms underlying the strong association between *SCN2A* loss of function and ASD and ID remains largely unknown.

In the neocortex, $Na_V1.2$ is primarily expressed in glutamatergic pyramidal cells (Hu et al., 2009; Li et al., 2014; Yamagata et al., 2017), where its distribution within different axonal compartments changes over development. In the first postnatal week in mice, corresponding to late gestation through the first year of life in humans (Workman et al., 2013), $Na_V1.2$ is the only sodium channel isoform expressed in the axon and AIS and is thus solely responsible for the initiation and propagation of APs (Gazina et al., 2015). Later in development, $Na_V1.2$ in the axon and distal AIS is replaced by $Na_V1.6$ (*SCN8A*), which has a lower voltage threshold for activation (Bender and Trussell, 2012; Kole and Stuart, 2012). Consequently, the distal AIS becomes the site of AP initiation, and $Na_V1.2$, now restricted to the proximal AIS, is thought to promote effective backpropagation of APs from the AIS into the soma (Hu et al., 2009). Given these potentially distinct developmental roles, it is critical to understand how *SCN2A* haploinsufficiency affects neuronal excitability and network function across development because this may shed light on ASD and ID etiology.

Here we examined cellular, synaptic, and behavioral consequences of heterozygous loss of *Scn2a* in mice ($Scn2a^{+/-}$). AP initiation was impaired in early development, consistent with a major role of *Scn2a* in axonal excitability. Unexpectedly, we identified deficits in somatodendritic excitability, consistent with the expression of $Na_V1.2$ channels throughout these compartments, that arose after early development and persisted

throughout life. Furthermore, postsynaptic features of excitatory synapses on *Scn2a*$^{+/-}$ neurons were both functionally and structurally altered in adulthood, with morphological and electrophysiological features reminiscent of less mature synapses. Synaptic impairments were found even when *Scn2a* expression was disrupted late in development, selectively impairing dendritic excitability without a period of reduced axonal excitability. Reduced dendritic excitability impaired the backpropagation of APs into distal dendrites, with corresponding deficits in spike timing-dependent plasticity. Finally, we observed sex-specific trends toward deficits in learning and sociability in *Scn2a*$^{+/-}$ mice. Together, these results identify a novel role of $Na_V1.2$ in the dendrites of mature pyramidal neurons, demonstrating that $Na_V1.2$ contributions to dendritic, but not only axonal, excitability are important for proper synaptic development and function. This generates the hypothesis that *SCN2A* contributes to ASD and ID by disrupting synaptic function, like many other ASD genes, and that these effects persist in mature neurons.

RESULTS

Scn2a Loss Impairs Axonal and Dendritic Excitability in Distinct Developmental Periods

To determine how *Scn2a* haploinsufficiency affects cortical neuron excitability, acute slices containing medial prefrontal cortex (mPFC) were prepared from *Scn2a*$^{+/-}$ and wild-type (WT) littermate control mice aged post-natal day 4 (P4) through P64. *Scn2a*$^{+/-}$ mice have a 50% reduction in $Na_V1.2$ mRNA and reduced Na_V-mediated currents in dissociated cell culture at P5–P9 (Planells-Cases et al., 2000) and are convulsive seizure free (Mishra et al., 2017; Ogiwara et al., 2018), consistent with the majority of *Scn2a* loss-of-function cases reported in ASD (Sanders et al., 2018). We focused our studies primarily on subcortically projecting layer 5b thick-tufted neurons that were identified based on electrophysiological properties (Clarkson et al., 2017; Dembrow et al., 2010; Gee et al., 2012) (STAR Methods) because dysfunction within this region and cell class has been implicated in ASD (Willsey et al., 2013). Neuronal excitability was assessed using a series of current steps to generate APs. The AP threshold was depolarized, and spike output was reduced relative to the WT in the first postnatal week (Figures 1A, 1C, and 1F). Differences between *Scn2a*$^{+/-}$ and the WT were not present thereafter (Figures 1B, 1C, and 1F), consistent with increased $Na_V1.6$ expression in the AIS. In agreement, persistent sodium currents, which reflect the recruitment of AIS sodium channels with the lowest threshold (Taddese and Bean, 2002), were suppressed in *Scn2a*$^{+/-}$ mice at P6 but not at P30 (Figures S1A–S1G). Furthermore, axonal conduction, assayed by imaging AP-evoked calcium transients in boutons, was reliable in both immature and mature neurons (Figure S2). Input resistance was comparable between *Scn2a*$^{+/-}$ and the WT at all ages, and transient and sustained potassium currents were not different in both immature and mature neurons (Figures S1H–S1K). Therefore, *Scn2a* haploinsufficiency impairs neuronal excitability early in development without functional compensation from the remaining *Scn2a* allele or other ion channels involved in AP initiation.

Although impairments in AP threshold recovered after P7, a closer examination of the AP waveform revealed a striking reduction in the velocity of the AP (dV/dt) that became more pronounced as neurons matured (Figures 1E and 1F) (>P22; WT: 578.2 ± 9.2 V/s, n = 44 cells; *Scn2a*$^{+/-}$: 417 ± 9.5, n = 33 cells; $p < 0.001$, Mann-Whitney test). Similar relative deficits were identified in putative thin-tufted neurons, which have different AP waveform characteristics compared which thick-tufted neurons (Dembrow et al., 2010) (>P18; WT: 426.9 ± 24.7 V/s, n = 8 cells; *Scn2a*$^{+/-}$: 358 ± 21.1, n = 9 cells; p = 0.007, Mann-Whitney test). Plotting AP velocity as a function of voltage (phase-plane) highlights two components of the rising phase of the AP (Figure 1D), as measured with somatic current clamp. The first relates to initiation of the AP in the AIS and the second to the recruitment of somatic sodium channels (Bean, 2007). In *Scn2a*$^{+/-}$ cells, both AIS and somatodendritic components of the AP were slower, suggesting that $Na_V1.2$ channels are distributed in both the AIS and somatodendritic compartment and that their density is lower in both compartments. Similar AP speed deficits were observed in pyramidal cells located in other neocortical regions, including the medial orbitofrontal cortex and primary visual cortex (Figure S3). In contrast to neocortical neurons, no alterations in AP threshold and peak speed were apparent in hippocampal CA1 pyramidal neurons (Figure S3). This is consistent with immunostaining indicating that hippocampal pyramidal cell dendrites predominantly express $Na_V1.6$ (Lorincz and Nusser, 2010).

Immunostaining for $Na_V1.2$ in the neocortex suggests that $Na_V1.2$ channels are predominantly localized to excitatory neurons, with little to no membrane localization observed in parvalbumin- or somatostatin-positive interneurons (Li et al., 2014; Yamagata et al., 2017). These cell classes instead express $Na_V1.1$ channels and exhibit hypoexcitability in *Scn1a* haploinsufficient mice aged P14–P21 (Favero et al., 2018; Tai et al., 2014). To further test whether $Na_V1.2$ contributes to AP excitability in these interneuron classes, we crossed *Scn2a*$^{+/+}$ and *Scn2a*$^{+/-}$ mice to mice engineered to express tdTomato in either parvalbumin- or somatostatin-positive cells (STAR Methods). Fluorescently guided whole-cell current clamp recordings were then made from these populations in slices prepared from P34–P40 animals (Figure 2). Although AP waveforms differed across cell class, neither peak dV/dt (Figure 2; PV peak dV/dt: WT: 336 ± 19 V/s, n = 9 cells, *Scn2a*$^{+/-}$: 326 ± 21 V/s, n = 9 cells; SOM peak dV/dt: WT: 362 ± 27 V/s, n = 12 cells, *Scn2a*$^{+/-}$: 313 ± 23 V/s, n = 11 cells; p = 0.43, $F_{genotype}(1,37) = 0.65$, 2-way ANOVA) or threshold (PV threshold: WT: −51.7 ± 1.6 mV, n = 9 cells, *Scn2a*$^{+/-}$: −51.9 ± 0.7 mV, n = 9 cells; SOM threshold: WT: −39.7 0.7 mV, n = 12 cells, *Scn2a*$^{+/-}$: −41.6 ± 1.0 mV, n = 11 cells; p = 0.41, $F_{genotype}(1,37) = 0.68$, 2-way ANOVA) were affected by loss of $Na_V1.2$.

Overall, these data indicate that *Scn2a* haploinsufficiency alters the excitability of neocortical pyramidal cells but not parvalbumin- or somatostatin-positive interneurons. Furthermore, within pyramidal cells, $Na_V1.2$ channels may be more consequential for somatodendritic excitability than axonal excitability. To explore the cellular consequences of reduced somatodendritic excitability, we modified an established computational model of cortical pyramidal cells (Hallermann et al., 2012) by

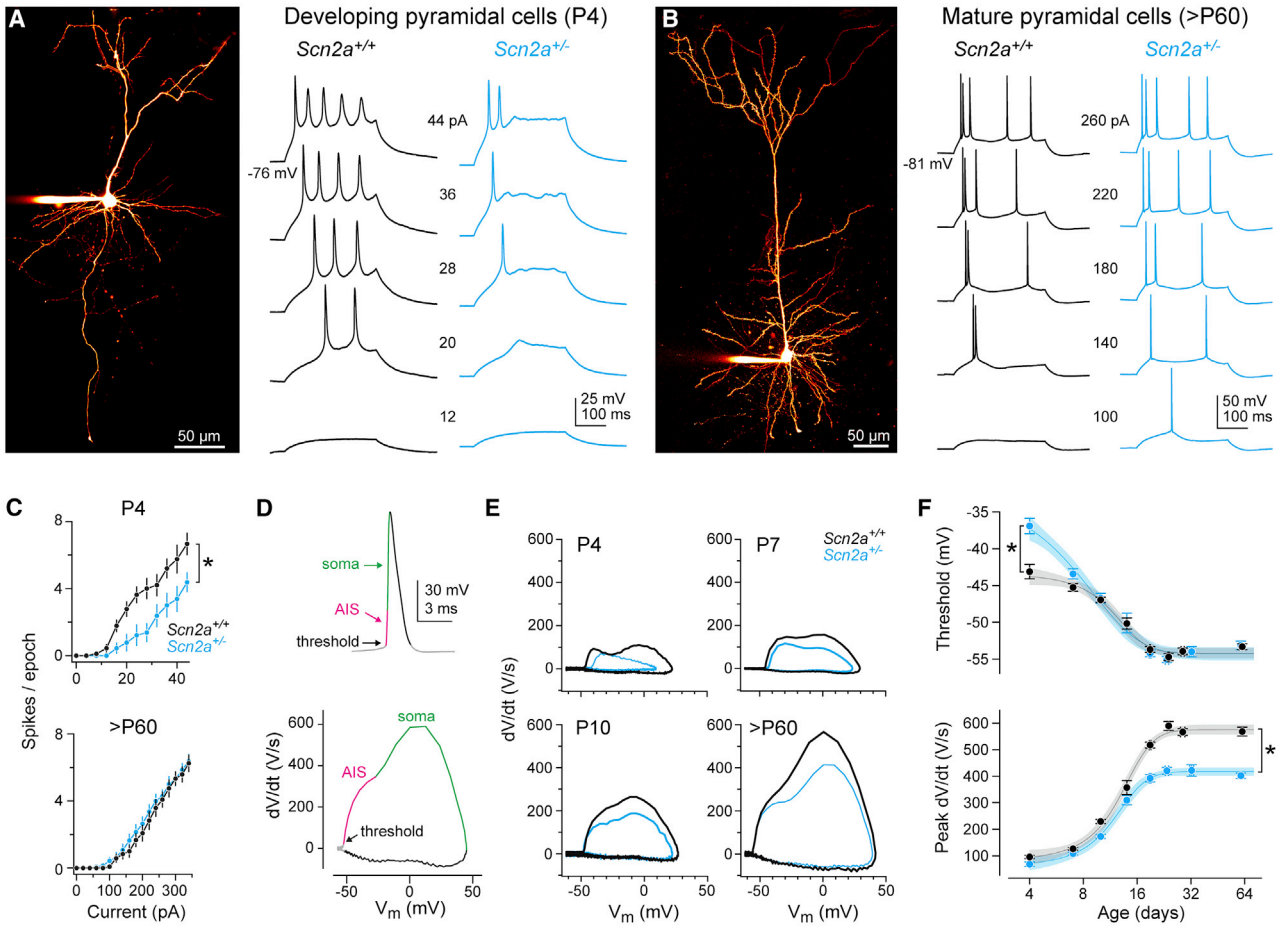

Figure 1. *Scn2a* Haploinsufficiency Impairs Different Aspects of Neuronal Excitability across Developmental Periods

(A) Left: 2-photon laser scanning microscopy (2PLSM) z stack of a developing pyramidal cell (P7). Right: APs generated by current injection (12–44 pA, 300 ms) in *Scn2a*$^{+/+}$ (black) and *Scn2a*$^{+/-}$ (cyan) cells. AP data are from neurons recorded at P4.

(B) Left: 2-photon z stack of a mature thick-tufted pyramidal cell. Right: AP response as in (A).

(C) APs (spikes) per 300-ms stimulation epoch for each current amplitude. At P4, *Scn2a*$^{+/-}$ cells are less excitable (firing rate slope between 4–44 pA; *Scn2a*$^{+/+}$: 0.67 ± 0.07 Hz/pA, n = 9 cells; *Scn2a*$^{+/-}$: 0.41 ± 0.07, n = 9 cells, *p = 0.02, Mann-Whitney test). After P60, no differences are observed between *Scn2a*$^{+/+}$ and *Scn2a*$^{+/-}$ cells (slope between 50–350 pA: *Scn2a*$^{+/+}$: 0.08 ± 0.007 Hz/pA, n = 12 cells; *Scn2a*$^{+/-}$: 0.08 ± 0.005, n = 14 cells, p = 0.96, Mann-Whitney test).

(D) An AP is plotted as voltage versus time (top) and dV/dt versus voltage (phase-plane plot; bottom). Different phases of the AP are color-coded across panels to indicate different phases of the AP corresponding to initiation of AP in AIS and full detonation of AP in the soma.

(E) Phase-plane plots at P4, P7, and P10 and after P60 in *Scn2a*$^{+/+}$ and *Scn2a*$^{+/-}$ cells. Note recovery of the AP threshold (kink) deficit between P4 and P10 and decrements in peak dV/dt that become more pronounced with age.

(F) Top: AP threshold across development from P4–P64 ($\log_2$ scale for age) in *Scn2a*$^{+/+}$ (black) and *Scn2a*$^{+/-}$ (cyan) mice. Bottom: peak rising phase dV/dt versus age. Circles and bars are mean ± SEM within an age group (n = 7–28 cells per group). Data fit with a generalized logistic function with 95% confidence intervals determined from fits to single cells. Asterisk indicates difference in parameters of the sigmoid fits. Top: left asymptote, *Scn2a*$^{+/+}$: −44.1 ± 0.6 mV, *Scn2a*$^{+/-}$ −35.6 ± 1.6, p < 0.001, unpaired t test. Bottom: right asymptote, *Scn2a*$^{+/+}$: 587.8 ± 10.2 V/s, *Scn2a*$^{+/-}$: 420.3 ± 9.5, p < 0.001, unpaired t test.

varying the localization and relative density of $Na_V1.2$ and $Na_V1.6$ (Ben-Shalom et al., 2017). First, $Na_V1.2$ channels were localized only to the AIS, and the AP waveform was compared between models with 100% and 50% $Na_V1.2$ expression (Figure 3A). The AP waveform was only modestly altered by such manipulations. To best account for empirical observations, we found that $Na_V1.2$ expression was required throughout the somatodendritic compartment, at equal levels with $Na_V1.6$ (Figure 3A; Figures S4A, S4B, S4E, and S4F). In this configuration, we modeled the AP waveform throughout the dendritic arbor and found that backpropagating APs (bAPs) from the AIS to the dendritic arbor were attenuated in a distance-dependent fashion. Although AP amplitudes were reduced only 10% in the soma, they were attenuated to far greater extents in distal dendrites (41% of the WT amplitude in the distal tuft) (Figures 3B and S4D), suggesting that cellular processes that depend on bAPs may be altered in *Scn2a*$^{+/-}$ cells.

Backpropagating APs can provide instructive signals for dendritic integration and synaptic plasticity, largely through their ability to elicit calcium influx through dendritic voltage-dependent calcium channels and N-methyl-D-aspartate (NMDA) receptors (Feldman, 2012; Larkum et al., 1999a; Stuart and

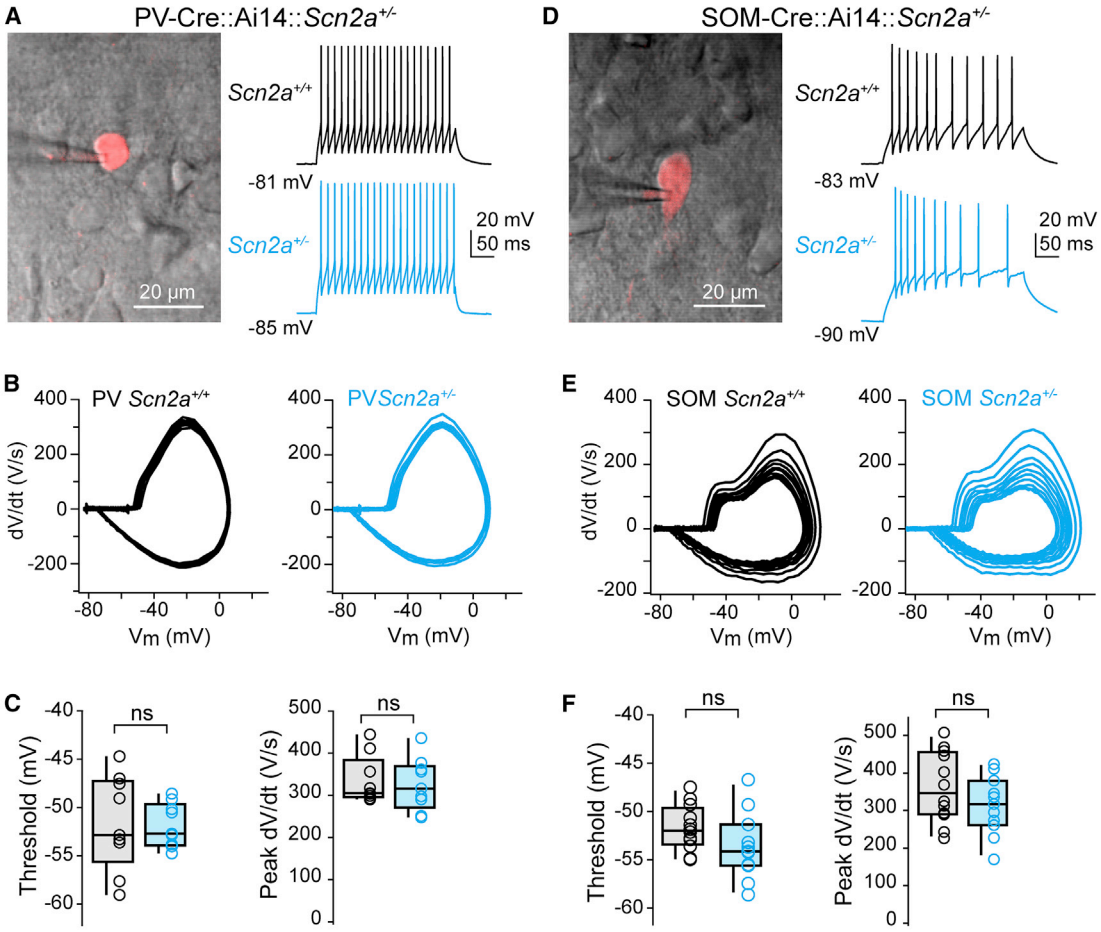

Figure 2. L5 Parvalbumin and Somatostatin Neuron APs Are Not Altered in *Scn2a*$^{+/-}$ Mice

(A) Right: 2PLSM single optical section of a tdTomato-positive parvalbumin-positive interneuron, overlaid with a scanning differential interference contrast (DIC) image showing the pipette in the cell-attached configuration. Scale bar, 20 µm. Left: spiking generated from parvalbumin-positive cells in *Scn2a*$^{+/+}$ and *Scn2a*$^{+/-}$ mice.

(B) Phase-plane plots of the data shown in (B).

(C) AP threshold and peak rising dV/dt for the first AP of the spike train. Open circles represent single cells. Boxplots are median, quartiles, and 90% tails. No statistical differences were noted. Data were obtained from P34–P40 animals.

(D) Right: 2PLSM single optical section of tdTomato-positive somatostatin-positive interneuron, overlaid with scanning-DIC image showing pipette in cell-attached configuration. Scale bar: 20 µm. Left: spiking generated from somatostatin-positive cells in *Scn2a*$^{+/+}$ and *Scn2a*$^{+/-}$ mice.

(E) Phase-plane plots of data shown in (D).

(F) AP threshold and peak rising dV/dt for the first AP of spike train. Open circles are single cells. Box plots are median, quartiles, and 90% tails. No statistical differences noted. Data were obtained from P37–P38 animals.

Häusser, 2001). To determine whether bAP-associated dendritic excitability was impaired in *Scn2a*$^{+/-}$ neurons, we imaged calcium transients evoked by trains of high-frequency bursts (2 APs at more than 100 Hz) at various locations throughout the apical dendrite of layer 5 (L5) pyramidal cells. Bursts of APs, rather than single APs, were chosen because they have been shown to evoke dendritic calcium transients throughout apical dendrites, including distal tuft regions (Barth et al., 2008; Gulledge and Stuart, 2003; Larkum et al., 1999b; Short et al., 2017). In WT neurons, bursts reliably evoked calcium transients throughout the apical dendrite. By contrast, calcium transients in *Scn2a*$^{+/-}$ neurons rapidly diminished in amplitude with increasing distance from the soma, becoming virtually absent in the most distal dendritic branches (Figures 3C and 3D). To determine whether these effects were due to acute loss of Na_V channels rather than a consequence of altered excitability during development, we partially blocked sodium channels in mature WT neurons with tetrodotoxin (TTX), using a concentration that mimicked the reduced AP speed observed in *Scn2a*$^{+/-}$ neurons (5 nM; Figures S4G and S4H). Consistent with acute effects of *Scn2a* haploinsufficiency, bAP-evoked calcium transients were reduced to a comparable extent in TTX-exposed WT neurons (Figures 3C and 3D). Thus, *Scn2a*$^{+/-}$ haploinsufficiency leads to a major persistent deficit in dendritic excitability in adult L5 neurons that is likely due to loss of $Na_V1.2$ channels localized to the dendrite.

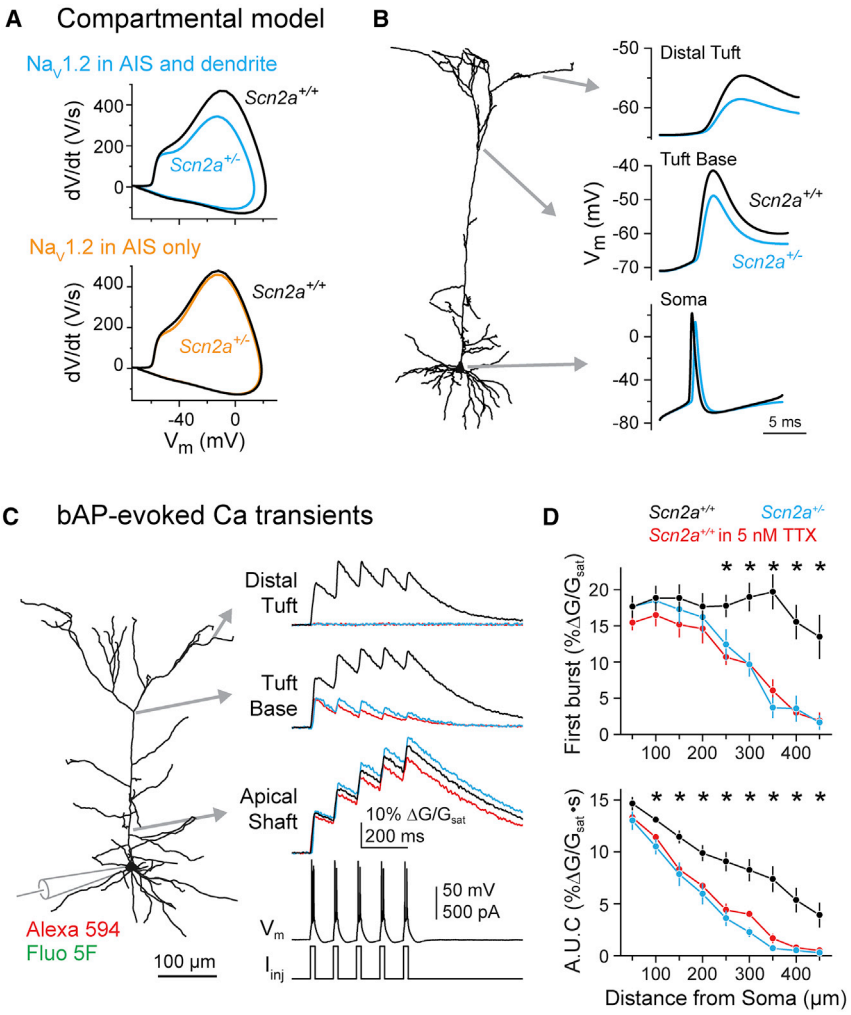

Figure 3. *Scn2a* Haploinsufficiency Impairs Dendritic Backpropagation of APs

(A) Compartmental model of a cortical L5 pyramidal cell with two distributions of $Na_V1.2$ and $Na_V1.6$ (see Figure S4 for other model configurations). The top model has $Na_V1.2$ in the proximal AIS, $Na_V1.6$ in the distal AIS, and $Na_V1.2$ and 1.6 equally co-expressed in the somatodendritic compartment. Note the reduction in peak rising dV/dt. The bottom model has $Na_V1.2$ in the proximal AIS only, with $Na_V1.6$ in the somatodendritic and distal AIS compartments. Removal of half of the $Na_V1.2$ channels results in only minor changes to the AP phase-plane.

(B) A single AP evoked in the top model in (A), backpropagating throughout the dendrite. More marked differences in AP shape were observed in more distal dendritic locations.

(C) 2PLSM calcium imaging throughout an apical dendrite of an L5 thick-tufted neuron. Calcium transients were evoked by bursts of AP doublets.

(D) Transient amplitude is plotted for the first of 5 bursts (top) and the area under the curve from stimulus onset to stimulus offset +100 ms (bottom) in *Scn2a*$^{+/+}$ (n = 10), *Scn2a*$^{+/-}$ (n = 8 cells), and *Scn2a*$^{+/+}$ cells treated with 5 nM TTX (n = 5). Circles and bars are means ± SEM. *p < 0.05, Kruskal-Wallis test.

Excitatory Synapses Are Impaired in Mature *Scn2a*$^{+/-}$ Neurons

Impairments of both axonal and dendritic excitability could affect synapses, which are a common locus of dysfunction in mouse models with ASD-associated genetic variants (Bourgeron, 2015; Monteiro and Feng, 2017; Tsai et al., 2012). We tested this by first measuring miniature excitatory postsynaptic currents (mEPSCs) and inhibitory postsynaptic currents (mIPSCs) at P6 and P27, capturing developmental periods of axonal and dendritic excitability deficits, respectively. Neither mEPSCs nor mIPSCs were affected at P6. At P27, mEPSC frequency was reduced by 48% (WT: 9.3 ± 1.1 Hz, n = 23 cells; Scn2a$^{+/-}$: 4.9 ± 0.8, n = 19 cells; p < 0.001 Mann-Whitney test), with no change in mEPSC amplitude (Figures 4A and 4B) or mIPSC amplitude or frequency (Figure S5A and S5B).

Lower mEPSC frequencies could reflect reductions in release probability or the number of functional synapses contributing to α-amino-3-hydroxy-5-methyl-4-isoxazolepropionic acid (AMPA)-mediated mEPSCs. The paired pulse ratio, which is sensitive to differences in release probability, was not different between *Scn2a*$^{+/-}$ and WT cells (Figures 4C, S5C, and S5D). By contrast, the ratio of AMPA- to NMDA-mediated current in evoked EPSCs was reduced in *Scn2a*$^{+/-}$ cells (Figure 4D; WT: 5.5 ± 0.7, n = 8 cells: *Scn2a*$^{+/-}$: 3.2 ± 0.2, n = 12 cells; p < 0.01, Mann-Whitney test). Taken together, the reduction in both mEPSC frequency and AMPA:NMDA ratio suggests that mature *Scn2a*$^{+/-}$ neurons have an excess of AMPA-lacking spines that are more commonly observed at earlier developmental time points (Hanse et al., 2013; Kerchner and Nicoll, 2008).

Consistent with these functional observations, dendritic spine morphology was also altered in mature but not immature *Scn2a*$^{+/-}$ cells, although, overall, the dendritic arbor structure was unaltered (Figures 5A and 5B). At P5–P6, filipodial spines identified on developing apical dendrites were similar in morphology and density in WT and *Scn2a*$^{+/-}$ neurons (Figures 5C and 5D). In more mature neurons (>P23), spine density was comparable between WT and *Scn2a*$^{+/-}$ on both apical and basal dendrites; however, *Scn2a*$^{+/-}$ spines were longer and had smaller heads relative to their total head and neck volume (Figures 5C and 5D), sharing features with spines more commonly found in less mature cells.

To determine whether impaired synaptic function was due to early developmental deficits in axonal excitability or persistent deficits in dendritic excitability, we engineered a mouse with one *Scn2a* allele under Cre-loxP control (*Scn2a*$^{+/fl}$) (Figure S6A). Mice were first crossed to the Ca^{2+}/calmodulin-dependent protein kinase IIα (CaMKIIα)-Cre driver line, which expresses Cre in neocortical pyramidal cells only after P10 (Figure S6B;

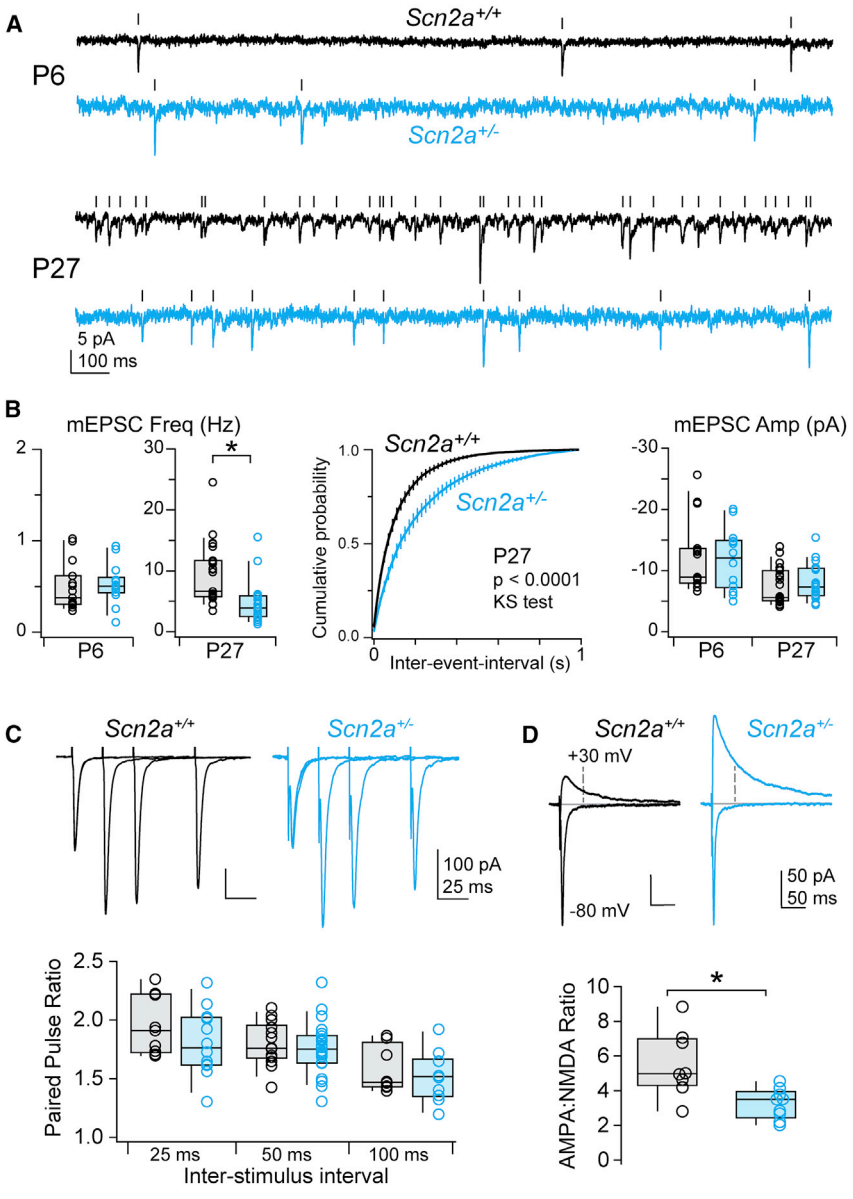

Figure 4. *Scn2a* Haploinsufficiency Disrupts Excitatory Synapse Function

(A) mEPSCs recorded in *Scn2a*$^{+/+}$ (black) and *Scn2a*$^{+/-}$ (cyan) pyramidal cells at P6 and P27. Tick marks denote detected events.

(B) Left: average mEPSC frequency per cell (open circles). Boxplots are median, quartiles, and 90% tails. Note that the frequency range is different for P6 and P27. Center: cumulative probability distribution of mEPSC event intervals at P27. Distributions were generated per cell and then averaged. Bars are SEM, $p < 0.0001$, Kolmogorov-Smirnov test. Right: average mEPSC amplitude per cell.

(C) Paired pulse ratio of evoked excitatory inputs to *Scn2a*$^{+/+}$ (black) and *Scn2a*$^{+/-}$ (cyan) pyramidal cells at 3 different stimulus intervals. Bottom: summary grouped by inter-stimulus interval. No differences were noted.

(D) Top: AMPA receptor-mediated and mixed AMPA and NMDA receptor-mediated evoked EPSCs at −80 and +30 mV, respectively. The dashed line denotes the time when the NMDA receptor-mediated component was calculated. Bottom: AMPA-NMDA ratio in *Scn2a*$^{+/+}$ and *Scn2a*$^{+/-}$ neurons. *$p < 0.01$, Mann-Whitney test.

Xu et al., 2000). Therefore, *Scn2a*$^{+/fl}$::CaMKIIα-Cre mice develop with normal AP threshold and spike output. In *Scn2a*$^{+/fl}$::CaMKIIα-Cre mice, peak dV/dt was not different at P18, likely because of a combination of low Cre expression and slow $Na_V1.2$ turnover. By P50, peak dV/dt matched constitutive *Scn2a*$^{+/-}$ neurons (Figure 6B). Furthermore, bAP-evoked dendritic Ca transients were suppressed to comparable extents, as observed in constitutive *Scn2a*$^{+/-}$ mice (Figures 6C and 6D). Thus, these mice developed without early deficits in axonal excitability and exhibited impaired dendritic excitability only later in development.

Strikingly, the AMPA:NMDA ratio was reduced in *Scn2a*$^{+/fl}$::CaMKIIα-Cre neurons when measured after P50, revealing that impaired dendritic excitability alone is sufficient to alter synapse strength (Figure 6E; WT: 4.2 ± 0.3, n = 12 cells; floxed: 2.5 ± 0.4, n = 11 cells; $p < 0.01$, Mann-Whitney test). To test whether these synaptic deficits result from a cell-autonomous loss of *Scn2a*, we injected a dilute Cre-expressing adeno-associated virus (AAV-EF1α-Cre-mCherry) into the mPFC of P28 *Scn2a*$^{+/fl}$ mice (Figure 6A). Four weeks later, we found that both peak dV/dt and the AMPA:NMDA ratio were reduced in Cre-positive but not Cre-negative neurons (Figures 6B and 6E; WT: 5.0 ± 0.4, n = 10 cells; floxed: 2.4 ± 0.4 n = 9 cells; $p < 0.01$, Mann-Whitney test). Modest increases in spine length were also noted in spines along the apical dendrites of *Scn2a*$^{+/fl}$::CaMKIIα-Cre cells (Figure S7). These results indicate that the persistent, cell-autonomous, dendritic function of $Na^V1.2$ is required to maintain aspects of normal synaptic function in mature pyramidal cells.

These changes in synapse structure and function could arise when synapses lack instructive signals for maintaining synaptic strength. Indeed, physiologically relevant forms of synaptic plasticity depend on the coincident detection of bAPs and glutamate at the synapse, a process that may be affected in *Scn2a*$^{+/-}$ cells (Feldman, 2012; Magee and Johnston, 1997; Markram et al., 1997, 2012). To test whether plasticity is impaired in these cells, we induced long-term potentiation (LTP) of putative apical dendrite synapses by pairing L1 fiber stimulation with bursts of APs (Figure 7A; Kampa et al., 2006; pairing protocol: Tzounopoulos et al., 2004). In WT neurons, paired stimulation resulted in long-lasting synaptic potentiation. By contrast, LTP was not observed in either *Scn2a*$^{+/-}$ neurons or in WT neurons in 5 nM

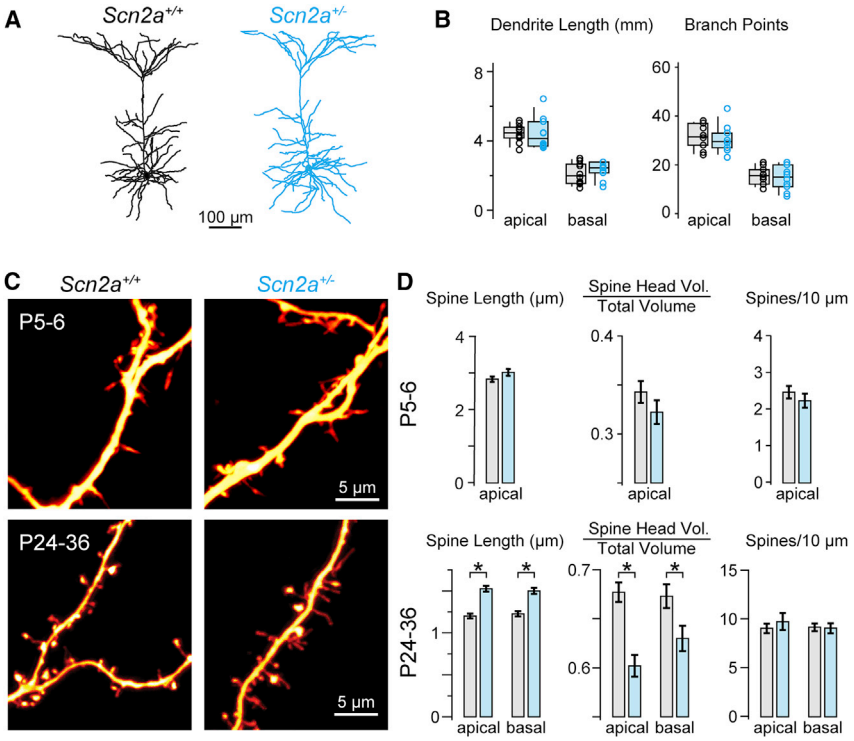

Figure 5. Dendritic Spines Are Morphologically Immature in *Scn2a*$^{+/-}$ Cells

(A) Examples of dendritic morphology in P22–P25 *Scn2a*$^{+/+}$ (black) and *Scn2a*$^{+/-}$ (cyan) pyramidal cells.

(B) Overall dendrite length and branch points in apical and basal trees. Open circles represent single cells. Boxplots are median, quartiles, and 90% tails. *Scn2a*$^{+/+}$, n = 10 cells; *Scn2a*$^{+/-}$, n = 10 cells. No differences across genotype were noted.

(C) Examples of spines along apical dendrites of immature (P5–P6) and more mature (P24–P36) neurons.

(D) Overall spine length from shaft to spine head, volume of the spine head relative to total volume of the head and shaft, and number of spines per length of dendrite were measured in apical dendrites of P5–P6 neurons (n = 560–685 spines per group, 1–4 dendritic branches per cells, 10 cells per group; note that basal dendrites often lacked spines at this age and were therefore not assessed). Spines along both apical and basal dendrites were imaged in P24–P36 neurons (n = 500–600 spines per group, 1–3 dendritic branches per cell, 6 cells per group). *p < 0.05, Mann-Whitney test.

TTX (Figures 7B–7D; excitatory postsynaptic potential [EPSP] slope normalized to baseline: WT: 1.52 ± 0.10, n = 11 cells; *Scn2a*$^{+/-}$: 0.98 ± 0.11, n = 11 cells; TTX: 0.97 ± 0.06, n = 9 cells; p = 0.0002, Kruskal-Wallis test; WT versus *Scn2a*$^{+/-}$: p = 0.0007, WT versus TTX: p = 0.002, Dunn's multiple comparisons test). Thus, *Scn2a* haploinsufficiency impairs synaptic plasticity, consistent with impairments in bAP-evoked calcium transients in dendrites.

Scn2a$^{+/-}$ Mice Have Trends toward Deficits in Learning and Social Behavior

Given these physiological deficits and the association of loss-of-function *SCN2A* mutations with ASD and ID in humans, we next asked whether *Scn2a* haploinsufficiency results in corresponding behavioral impairments in mice. Because mouse models harboring other ASD-associated genetic variants exhibit a range of behavioral differences (Pasciuto et al., 2015; Silverman et al., 2010), we screened *Scn2a*$^{+/-}$ mice and WT littermates of both sexes (5–13 mice per sex and genotype combination) through a behavioral panel designed to assess locomotion, anxiety, repetitive behavior, sociability, and learning (Figure S8). In total, 10 assays were performed, yielding 30 metrics that we assessed for genotypic differences. Although no individual metric differed significantly between the WT and heterozygote mouse after correcting for multiple comparisons, we observed a trend toward impaired reversal learning in a water T maze task in males (Figure S8A). In this task, mice must first learn which arm of a maze contains a submerged platform (days 1–4, 4 trials/day) and then reverse their association when the platform location is switched (days 5–8, 6 trials/day). A replication experiment of two further batches of male (23 versus 24 mice total) and female (20 versus 24 mice total) *Scn2a*$^{+/-}$ and WT littermates showed a similar trend toward reversal learning impairments (Figure S9A; p = 0.026, $F_{genotype}$ (1,45) = 5.2, 2-way repeated-measures ANOVA; alpha required for multiple comparisons in replication cohort: 0.003), whereas no trends were observed in females.

We also observed trends suggestive of social impairments in female mice (Figures S9B–S9D). Specifically, in our initial screen, we observed no difference in social approach behavior in a two-chamber social task, where mice had the option of interacting with a caged, sex-matched stimulus mouse in one chamber or an inanimate toy mouse in the other (Figure S8B). In a second cohort, mice were paired with the same stimulus mouse for three trials to assess social approach and habituation. Both sexes and genotypes showed a comparable preference for the stimulus mouse versus the toy mouse across the three trials (Figure S8B). Given the importance of social interaction in ASD, we also tested interactions when the toy mouse was replaced with a novel stimulus mouse on the fourth trial. Both male and female WT mice switched preference to the new stimulus mouse, whereas female *Scn2a*$^{+/-}$ mice showed no preference for the novel mouse (Δinteraction time: *Scn2a*$^{+/+}$: −17.1 ± 4.1 s, n = 13 mice; *Scn2a*$^{+/+}$: 9.3 ± 10.3 s, n = 8 mice, p = 0.017; Mann-Whitney test) (Figure S9D). Female *Scn2a*$^{+/-}$ mice were also found to enter the open arms of the elevated plus maze more often (percent time in open arms: *Scn2a*$^{+/+}$: 22.9% ± 2.1%, n = 24 mice; *Scn2a*$^{+/+}$: 34.3% ± 2.7%, n = 20 mice, p = 0.002; Mann-Whitney test), with a trend toward spending more time in these open arms (number of open arm entries: *Scn2a*$^{+/+}$: 56.6 ± 3.3, n = 24 mice; *Scn2a*$^{+/-}$: 73.6 ± 5.5 n = 20, p = 0.012; Mann-Whitney test) (Figure S9F). Overall, these data suggest that *Scn2a*$^{+/-}$ mice may display sex-specific impairments in behavioral flexibility and social discrimination.

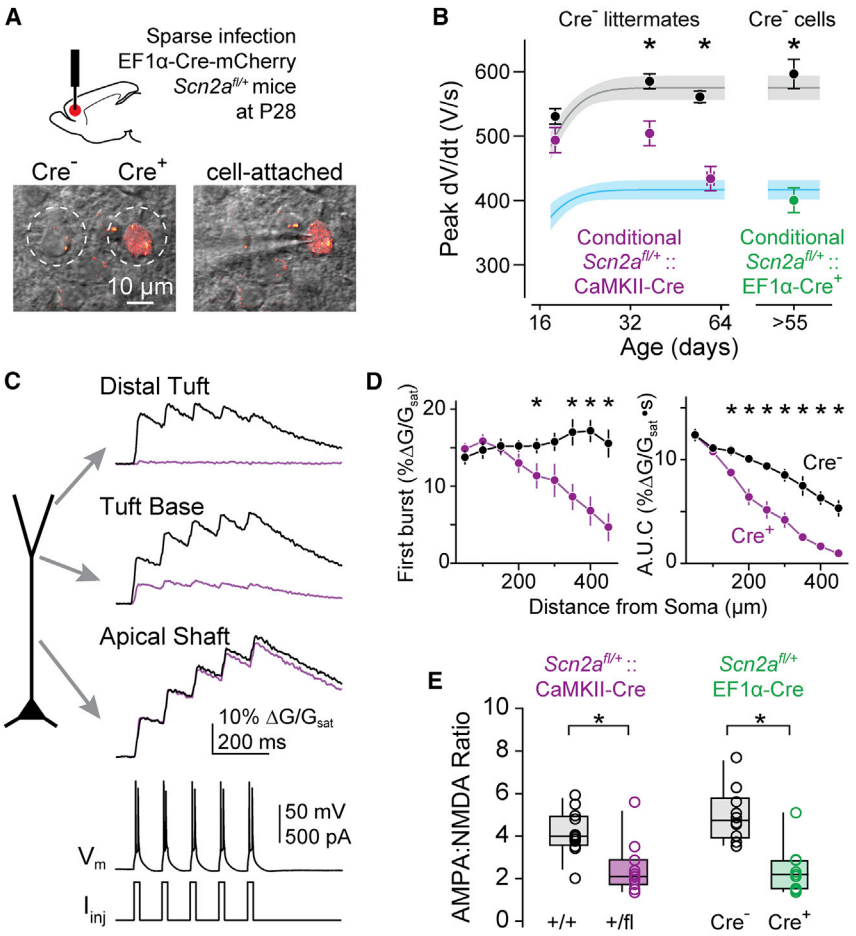

Figure 6. Inducing *Scn2a* Haploinsufficiency Late in Development Disrupts Dendritic Excitability, AP Backpropagation, and Synaptic Stability

(A) *Scn2a*$^{+/fl}$ mice were injected with a dilute Cre virus, infecting a subset of neurons in the PFC. Images are single 2PLSM optical sections of transmitted laser light (scanning DIC) and mCherry fluorescence (red). Left: dashed circles highlight two neighboring Cre+ and Cre− neurons. Right: Cre+ neuron targeted for whole-cell recording with the pipette from the left side. The image was taken while in the cell-attached configuration.

(B) Peak dV/dt versus age in conditional *Scn2a* mice. dV/dt measurements were made from CaMKII::*Scn2a*$^{+/fl}$ or *Scn2a*$^{+/+}$ mice at several ages and compared with a developmental curve derived from constitutive mice. Note the overlap with the WT developmental curve at P18 and the eventual overlap with the *Scn2a*$^{+/-}$ curve after P50 for CaMKII::*Scn2a*$^{+/fl}$ neurons. Neurons in *Scn2a*$^{+/fl}$ mice injected with dilute Cre virus were assessed after P55. Circles and bars are means ± SEM. *p < 0.01, Mann-Whitney test.

(C) Dendritic calcium imaging as in Figure 3C, except in CaMKII::*Scn2a*$^{+/fl}$ or *Scn2a*$^{+/+}$ cells.

(D) Transient amplitude is plotted for the first of 5 bursts (left) and area under the curve from stimulus onset to stimulus onset + 500 ms (right) in CaMKII::*Scn2a*$^{+/+}$ (n = 9 cells) or CaMKII::*Scn2a*$^{+/-}$ (n = 8 cells). Circles and bars are means ± SEM. *p < 0.05, Mann-Whitney test.

(E) AMPA:NMDA ratio between CaMK-Cre:*Scn2a*$^{+/+}$ and *Scn2a*$^{+/fl}$ littermates and between Cre+ and Cre− neurons in *Scn2a*$^{+/fl}$ mice injected with EF1α-Cre. *p < 0.05, Mann-Whitney test.

DISCUSSION

Here we report that $Na_V1.2$ channels contribute to excitatory synapse function through an unexpected role in dendritic excitability and that cell-autonomous *Scn2a* haploinsufficiency late in development is sufficient to impair excitatory synaptic connectivity. This reframes *SCN2A* as a gene not only important for axonal excitability but also for dendritic excitability in neocortical pyramidal neurons. *Scn2a* haploinsufficiency affects dendritic excitability throughout life, with corresponding deficits in synaptic function and plasticity that may be consequential for ASD and ID etiology.

$Na_V1.2$ Channel Expression in Neocortical Pyramidal Cell Dendrites

Although the expression of $Na_V1.2$ in the AIS is well established (Gazina et al., 2015; Hu et al., 2009; Liao et al., 2010), there is less consensus on its distribution in pyramidal cell dendrites. The first immunostaining of $Na_V1.2$ in the neocortex revealed somatic and apical dendritic localization in pyramidal cells, although this may represent a pool of newly synthesized channels within vesicles (Gong et al., 1999). Functionally, somatodendritic Na_V currents in neocortical pyramidal neurons are best described by $Na_V1.2$ channels (Hu and Bean, 2018; Hu et al., 2009). Here we found that the AP waveform was altered in constitutive and conditional *Scn2a*$^{+/-}$ prefrontal thick-tufted L5 pyramidal cells in a manner best explained by somatodendritic loss of $Na_V1.2$, with no functional compensation from the residual *Scn2a* allele or $Na_V1.6$ (Figures 1, 2, S1, and S4). Similar observations were made in prefrontal thin-tufted L5 pyramidal cells and in thick-tufted L5 pyramidal cells localized to the orbitofrontal and primary visual cortex (Figure S3). Moreover, AP-evoked calcium transients in PFC pyramidal neurons were suppressed throughout the dendritic arbor of *Scn2a*$^{+/-}$ cells (Figures 3 and 6), and this effect could be mimicked in WT neurons acutely by sub-saturating concentrations of TTX.

In mature hippocampal preparations, $Na_V1.2$ channels have been visualized in pyramidal cell initial segments and were also co-localized with the presynaptic terminal marker VGlut1 in strata containing unmyelinated axons, but were not present in pyramidal cell dendrites (Lorincz and Nusser, 2010, but see Johnson et al., 2017). Consistent with this observation, the AP waveform was not altered in recordings from CA1 hippocampal neurons (Figure S3). This suggests that $Na_V1.2$ channels are selectively found in the dendrites of neocortical but not archicortical pyramidal cells. This hypothesis will require further work to measure dendritic excitability directly in hippocampal neurons and to rule out compensation by other Na_V subtypes.

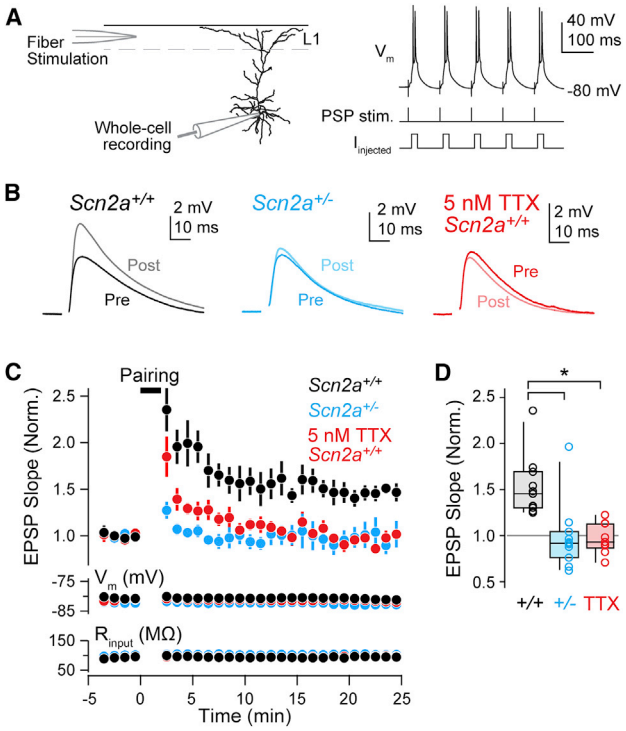

Figure 7. *Scn2a* Haploinsufficiency Impairs Synaptic Plasticity

(A) Recording configuration for burst-based LTP experiments. A stimulating electrode was placed in L1, and synaptic stimulation was paired with somatic current-evoked AP bursts.

(B) Example of EPSPs before and after the LTP pairing protocol. Lighter shades indicate post-induction data (15–25 min after pairing). Stimulus artifact was removed for clarity.

(C) EPSP slope (first 2 ms), membrane potential (V_m), and input resistance (R_{in}) versus time before and after LTP induction. Circles and bars are mean ± SEM.

(D) EPSC slope per cell in *Scn2a*$^{+/+}$ cells with and without TTX and *Scn2a*$^{+/-}$ cells. *p = 0.0002, Kruskal-Wallis test; WT versus *Scn2a*$^{+/-}$: p = 0.0007, WT versus TTX: p = 0.002, Dunn's multiple comparisons test.

Furthermore, there may be regional differences in expression in other neocortical regions between the frontal and visual cortex or in other laminae. Altogether, these data indicate that $Na_V1.2$ is functionally expressed in the somata and dendrites of neocortical pyramidal neurons, where they play an important role in excitability and synapse function.

Role of $Na_V1.2$ in Dendritic and Synaptic Function

Scn2a haploinsufficiency selectively impairs dendritic excitability and synaptic function in mature PFC pyramidal cells with no effects on AP initiation or propagation (Figures 1 and S2). This distinguishes $Na_V1.2$ from other Na_V isoforms expressed in the mature cortex that either support overall excitability in inhibitory neurons ($Na_V1.1$) or contribute to both AP generation and dendritic excitability in pyramidal neurons ($Na_V1.6$) (Hu et al., 2009; Lorincz and Nusser, 2008; Ogiwara et al., 2007). In the mature brain, $Na_V1.2$ may instead play a major role in supporting the backpropagation of APs within neocortical pyramidal cell dendrites. These bAPs depolarize dendrites and can contribute to the generation of dendritic spikes, especially when paired with local synaptic stimulation (Larkum et al., 1999a) or when packaged in high-frequency bursts (Barth et al., 2008; Gulledge and Stuart, 2003; Larkum et al., 1999b). Here we found that somatodendritic $Na_V1.2$ channels are critical for supporting bAPs from the AIS to the distal dendrites and that *Scn2a* haploinsufficiency impairs the ability to induce a burst-based form of associative spike timing-dependent plasticity at apical tuft synapses (Figures 3C and 3D). Furthermore, excitatory synapse function was altered in ways most consistent with a postsynaptic, dendritic role of $Na_V1.2$ channels in mature neurons. Presynaptic metrics, including the likelihood of evoking calcium transients in axonal boutons and paired-pulse ratio, were unaffected by *Scn2a* loss (Figures S2 and S5). By contrast, the mEPSC frequency and AMPA:NMDA ratio were reduced, consistent with the hypothesis that a higher proportion of silent synapses are present in *Scn2a*$^{+/-}$ cells (Figure 4). These effects were mirrored by structural differences in spines imaged on basal and apical dendrites of more mature neurons (Figures 5C and 5D). Interestingly, these functional and structural aspects were dissociable because induction of *Scn2a* haploinsufficiency late in life reduced the AMPA:NMDA ratio with little change in spine shape (Figures 6E and S7). This is consistent with other cell- and circuit-based perturbations in more mature neurons, where synapse strength can be altered markedly with relatively small changes in spine morphology (Dobi et al., 2011; Sala et al., 2003; Shen et al., 2014), and suggests that certain aspects of spine morphology are developmentally regulated before the ages at which *Scn2a* loss was induced in the *Scn2a*$^{+/fl}$ mice studied here.

Although we focused on backpropagation of bursts and related plasticity in the tuft of *Scn2a*$^{+/-}$ cells, reductions in $Na_V1.2$ density likely affect many other dendritic processes. For example, dendrites are capable of generating spikes independent of APs at the AIS through multiple mechanisms, including Na_Vs (Kim et al., 2015; Stuart et al., 1997). These dendritic spikes alone can be instructive for synaptic plasticity (Golding et al., 2002; Kampa et al., 2007). Furthermore, plasticity mechanisms that influence synaptic strength in dendrites more proximal to the soma are also likely affected, given the structural changes observed in basal dendrites and in EPSCs evoked with electrical stimulation in L5. The high-frequency burst-based stimuli used here readily produced calcium transients in proximal dendritic locations in *Scn2a*$^{+/-}$ cells. Other activity that drives dendritic calcium influx, including single APs or coordinated activation of excitatory inputs (Ariav et al., 2003), may instead be affected in these regions.

Measurements of persistent sodium current suggest that the loss of $Na_V1.2$ channels is not functionally compensated for by $Na_V1.6$. Consistent with this, mRNAs for $Na_V1.6$, $Na_V1.1$, and Na_V β subunits are unaltered in *Scn2a*$^{+/-}$ mice (Ogiwara et al., 2018). We also found no differences in transient or sustained potassium currents or input resistance, suggesting that other channel types are similarly unaltered by $Na_V1.2$ reductions. However, interpretation of this is hampered by the inability to adequately clamp these currents via somatic recording. Although empirical measurements indicate that we have reasonable voltage control over persistent sodium currents in the AIS (Figures S1E–S1G), other events, including synaptic activity and potassium currents,

may suffer from incomplete voltage control in these large dendritic cells (Beaulieu-Laroche and Harnett, 2018; Williams and Mitchell, 2008). Importantly, voltage errors are likely comparable across genotype because we did not observe differences in dendritic morphology, input resistance, and spine density (Figures 5 and S1). Furthermore, the effects of $Na_V1.2$ loss on bAP-associated dendritic calcium transients were recapitulated by acutely blocking a small fraction of Na_Vs in WT cells. Thus, even though we have not assessed the function of ion channels in the apical tuft directly, our data are most easily explained by a reduction in $Na_V1.2$ alone, with no compensation from other Na_Vs or other ion channel classes.

Relationship with Other ASD-Associated Genes

Although *SCN2A*'s ASD association has been established for some time (Sanders et al., 2012), the mechanistic underpinnings of this strong association have been a mystery. Because $Na_V1.2$ channels are best understood for their role in AP initiation (Hu et al., 2009), it was difficult to find parallels with other ASD-associated genes that are associated with synaptic function and gene transcription (De Rubeis et al., 2014). The data shown here instead suggest that *SCN2A* function in ASD converges at the dendrite, with the large group of ASD-associated genes involved in synaptic function. Indeed, disruptions in both excitatory synaptic function and neuronal excitability have been reported in other ASD-associated genes (Bateup et al., 2011; Bozdagi et al., 2010; Contractor et al., 2015; Greer et al., 2010; Meredith and Mansvelder, 2010; Nestor and Hoffman, 2012; Williams et al., 2015; Yashiro et al., 2009; Yi et al., 2016). How the other ASD-associated genes with roles in regulating gene expression mediate ASD risk remains unknown (Sanders, 2015); however, we note that *SCN2A* has been reported to be a regulatory target of both FMRP and CHD8 (Darnell et al., 2011; Golden et al., 2019; Sugathan et al., 2014).

SCN2A was one of the first genes identified with a clear excess of missense mutations in addition to predicted protein-truncating variants linked to ASD and ID (Ben-Shalom et al., 2017; Sanders et al., 2015). Recent efforts have identified other genes harboring ASD-associated missense variants, although the functional implications of such mutations are largely unclear (Geisheker et al., 2017). $Na_V1.2$ function, by contrast, can be well characterized, allowing for a better understanding of how missense mutations that alter channel activity affect neuronal function. Several recurring *SCN2A* missense variants block sodium flux (Begemann et al., 2019; Ben-Shalom et al., 2017). These may be functionally identical to protein-truncating variants because we and others found that $Na_V1.2$ function is reduced 50% in *Scn2a*$^{+/-}$ mice (Planells-Cases et al., 2000), with no evidence of functional compensation. Other *SCN2A* missense variants observed in ASD patients alter channel voltage dependence or kinetics, reducing neuronal excitability in models of developing cortical pyramidal cells (Ben-Shalom et al., 2017). Whether they result in similar dendritic deficits in mature neurons remains to be tested.

Role of *Scn2a* in Learning and Behavior

The behavioral differences observed so far in heterozygous *Scn2a* mice parallel aspects of behavioral phenotypes reported in other mouse models of ASD-associated genes (Pasciuto et al., 2015; Silverman et al., 2010). Here we observed trends toward impaired behavioral flexibility in males and impaired social recall and reduced anxiety in females. Reversal learning effects we observed in male mice parallel spatial learning impairments observed previously in male *Scn2a*$^{+/-}$ mice (Middleton et al., 2018). Whether female *Scn2a*$^{+/-}$ mice are similarly resistant to these specific spatial learning impairments has not been explored. Male *Scn2a*$^{+/-}$ mice were also recently found to display novelty-induced exploratory hyperactivity, social behavior impairment, enhanced fear conditioning, and deficient fear extinction (Tatsukawa et al., 2019). Of note, several phenotypic results, including open field, elevated plus maze, and social interaction, were not replicated here. This issue of reproducibility is unfortunately common in behavioral studies examining ASD-like phenotypes in the mouse and may relate to differences in genetic background, genetic drift over generations, or experimental conditions (Brunner et al., 2015; Chadman et al., 2008; Ey et al., 2012; Spencer et al., 2011).

Children with *SCN2A* loss-of-function variants display a range of phenotypes, including ASD, ID, and cortical visual impairments. Here we found that neurons in the visual cortex have similar deficits in AP waveform, possibly reflecting deficits in dendritic excitability that could impair visual processing (Xu et al., 2012). Furthermore, a fraction of these children also develop seizure phenotypes, typically after the first year of life (Sanders et al., 2018; Wolff et al., 2017). *Scn2a*$^{+/-}$ mice have been reported to be seizure free (Mishra et al., 2017; Planells-Cases et al., 2000) or to have low-frequency, short-duration spike wave discharges (Ogiwara et al., 2018). The variability of seizure occurrence in humans and mice suggests that factors other than *Scn2a* loss alone, including genetic background, may contribute to seizure susceptibility.

In conclusion, we found that haploinsufficiency induction at two different developmental time points, both well after $Na_V1.2$ channels cease to contribute to AP initiation, was sufficient to alter synaptic function (Figures 3 and 6). Although this result does not exclude additional effects on network function because of reduced axonal excitability in early cortical development, it does indicate that proper $Na_V1.2$ function that supports dendritic excitability is required for maintaining synaptic strength. Thus, restoring proper $Na_V1.2$ function, even in the mature brain, may be an enticing avenue for therapeutic intervention in loss-of-function *SCN2A* cases.

STAR★METHODS

Detailed methods are provided in the online version of this paper and include the following:

- KEY RESOURCES TABLE
- LEAD CONTACT AND MATERIALS AVAILABILITY
- EXPERIMENTAL MODEL AND SUBJECT DETAILS
- METHOD DETAILS
  - *Ex Vivo* Electrophysiology
  - Two-Photon Imaging
  - Behavioral Analyses
  - Modeling
  - Chemicals
- QUANTIFICATION AND STATISTICAL ANALYSIS

SUPPLEMENTAL INFORMATION

Supplemental Information can be found online at https://doi.org/10.1016/j.neuron.2019.05.037.

ACKNOWLEDGMENTS

We are grateful to Drs. E. Glasscock and M. Montal for providing *Scn2a*$^{+/-}$ mice and Drs. G. Davis, K. Kay, D. Manoli, and M. Scanziani and members of the Bender and Sanders labs for critically assessing this work. Behavioral data were obtained with the help of Dr. M. Gill and the Gladstone Institute Neurobehavioral Core. CaMKII-Cre::Ai14 image acquisition and analysis of dendritic spines was performed at the Gladstone Institute Histology and Light Microscopy Core. This research was supported by SFARI grant 513133 (to K.J.B.), a Natural Sciences and Engineering Research Council (NSERC) of Canada PGS-D scholarship (to P.W.E.S.), and NIH grants F32 NS095580 (to R.B.S.) and R01 MH110928 (to S.J.S.).

AUTHOR CONTRIBUTIONS

Conceptualization, P.W.E.S., R.B.-S., S.J.S., and K.J.B.; methodology, P.W.E.S., R.B.-S., and K.J.B.; software, P.W.E.S., R.B.-S., K.J.B., Jr., and R.L.C.; formal analysis, P.W.E.S., R.B.-S., C.M.K., and K.J.B.; investigation, P.W.E.S., R.B.-S., C.M.K., K.J.B., Jr., and K.J.B.; resources, S.J.S. and K.J.B.; writing – original draft, P.W.E.S. and K.J.B.; writing – review and editing, all authors; visualization, P.W.E.S., R.B.-S., and K.J.B.; supervision, K.J.B.; project administration, S.J.S. and K.J.B.; and funding acquisition, P.W.E.S., R.B.-S., S.J.S., and K.J.B.

DECLARATION OF INTERESTS

The authors declare no competing interests.

Received: July 3, 2018
Revised: March 23, 2019
Accepted: May 22, 2019
Published: June 20, 2019

REFERENCES

Ariav, G., Polsky, A., and Schiller, J. (2003). Submillisecond precision of the input-output transformation function mediated by fast sodium dendritic spikes in basal dendrites of CA1 pyramidal neurons. J. Neurosci. *23*, 7750–7758.

Barth, A.M.I., Vizi, E.S., Zelles, T., and Lendvai, B. (2008). α_2-adrenergic receptors modify dendritic spike generation via HCN channels in the prefrontal cortex. J. Neurophysiol. *99*, 394–401.

Bateup, H.S., Takasaki, K.T., Saulnier, J.L., Denefrio, C.L., and Sabatini, B.L. (2011). Loss of Tsc1 in vivo impairs hippocampal mGluR-LTD and increases excitatory synaptic function. J. Neurosci. *31*, 8862–8869.

Bean, B.P. (2007). The action potential in mammalian central neurons. Nat. Rev. Neurosci. *8*, 451–465.

Beaulieu-Laroche, L., and Harnett, M.T. (2018). Dendritic Spines Prevent Synaptic Voltage Clamp. Neuron *97*, 75–82.e3.

Begemann, A., Acuña, M.A., Zweier, M., Vincent, M., Steindl, K., Bachmann-Gagescu, R., Hackenberg, A., Abela, L., Plecko, B., Kroell-Seger, J., et al. (2019). Further corroboration of distinct functional features in SCN2A variants causing intellectual disability or epileptic phenotypes. Mol. Med. *25*, 6.

Ben-Shalom, R., Keeshen, C.M., Berrios, K.N., An, J.Y., Sanders, S.J., and Bender, K.J. (2017). Opposing Effects on $Na_V1.2$ Function Underlie Differences Between SCN2A Variants Observed in Individuals With Autism Spectrum Disorder or Infantile Seizures. Biol. Psychiatry *82*, 224–232.

Bender, K.J., and Trussell, L.O. (2009). Axon initial segment Ca2+ channels influence action potential generation and timing. Neuron *61*, 259–271.

Bender, K.J., and Trussell, L.O. (2012). The physiology of the axon initial segment. Annu. Rev. Neurosci. *35*, 249–265.

Bourgeron, T. (2015). From the genetic architecture to synaptic plasticity in autism spectrum disorder. Nat. Rev. Neurosci. *16*, 551–563.

Bozdagi, O., Sakurai, T., Papapetrou, D., Wang, X., Dickstein, D.L., Takahashi, N., Kajiwara, Y., Yang, M., Katz, A.M., Scattoni, M.L., et al. (2010). Haploinsufficiency of the autism-associated Shank3 gene leads to deficits in synaptic function, social interaction, and social communication. Mol. Autism *1*, 15.

Brunner, D., Kabitzke, P., He, D., Cox, K., Thiede, L., Hanania, T., Sabath, E., Alexandrov, V., Saxe, M., Peles, E., et al. (2015). Comprehensive Analysis of the 16p11.2 Deletion and Null Cntnap2 Mouse Models of Autism Spectrum Disorder. PLoS ONE *10*, e0134572.

Cánovas, J., Berndt, F.A., Sepúlveda, H., Aguilar, R., Veloso, F.A., Montecino, M., Oliva, C., Maass, J.C., Sierralta, J., and Kukuljan, M. (2015). The Specification of Cortical Subcerebral Projection Neurons Depends on the Direct Repression of TBR1 by CTIP1/BCL11a. J. Neurosci. *35*, 7552–7564.

Chadman, K.K., Gong, S., Scattoni, M.L., Boltuck, S.E., Gandhy, S.U., Heintz, N., and Crawley, J.N. (2008). Minimal aberrant behavioral phenotypes of neuroligin-3 R451C knockin mice. Autism Res. *1*, 147–158.

Clarkson, R.L., Liptak, A.T., Gee, S.M., Sohal, V.S., and Bender, K.J. (2017). D3 Receptors Regulate Excitability in a Unique Class of Prefrontal Pyramidal Cells. J. Neurosci. *37*, 5846–5860.

Contractor, A., Klyachko, V.A., and Portera-Cailliau, C. (2015). Altered Neuronal and Circuit Excitability in Fragile X Syndrome. Neuron *87*, 699–715.

Coupé, P., Munz, M., Manjón, J.V., Ruthazer, E.S., and Collins, D.L. (2012). A CANDLE for a deeper in vivo insight. Med. Image Anal. *16*, 849–864.

Darnell, J.C., Van Driesche, S.J., Zhang, C., Hung, K.Y.S., Mele, A., Fraser, C.E., Stone, E.F., Chen, C., Fak, J.J., Chi, S.W., et al. (2011). FMRP stalls ribosomal translocation on mRNAs linked to synaptic function and autism. Cell *146*, 247–261.

De Rubeis, S., He, X., Goldberg, A.P., Poultney, C.S., Samocha, K., Cicek, A.E., Kou, Y., Liu, L., Fromer, M., Walker, S., et al.; DDD Study; Homozygosity Mapping Collaborative for Autism; UK10K Consortium (2014). Synaptic, transcriptional and chromatin genes disrupted in autism. Nature *515*, 209–215.

Dembrow, N.C., Chitwood, R.A., and Johnston, D. (2010). Projection-specific neuromodulation of medial prefrontal cortex neurons. J. Neurosci. *30*, 16922–16937.

Dobi, A., Seabold, G.K., Christensen, C.H., Bock, R., and Alvarez, V.A. (2011). Cocaine-induced plasticity in the nucleus accumbens is cell specific and develops without prolonged withdrawal. J. Neurosci. *31*, 1895–1904.

Ey, E., Yang, M., Katz, A.M., Woldeyohannes, L., Silverman, J.L., Leblond, C.S., Faure, P., Torquet, N., Le Sourd, A.M., Bourgeron, T., and Crawley, J.N. (2012). Absence of deficits in social behaviors and ultrasonic vocalizations in later generations of mice lacking neuroligin4. Genes Brain Behav. *11*, 928–941.

Favero, M., Sotuyo, N.P., Lopez, E., Kearney, J.A., and Goldberg, E.M. (2018). A Transient Developmental Window of Fast-Spiking Interneuron Dysfunction in a Mouse Model of Dravet Syndrome. J. Neurosci. *38*, 7912–7927.

Feldman, D.E. (2012). The spike-timing dependence of plasticity. Neuron *75*, 556–571.

Gazina, E.V., Leaw, B.T.W., Richards, K.L., Wimmer, V.C., Kim, T.H., Aumann, T.D., Featherby, T.J., Churilov, L., Hammond, V.E., Reid, C.A., and Petrou, S. (2015). 'Neonatal' Nav1.2 reduces neuronal excitability and affects seizure susceptibility and behaviour. Hum. Mol. Genet. *24*, 1457–1468.

Gee, S., Ellwood, I., Patel, T., Luongo, F., Deisseroth, K., and Sohal, V.S. (2012). Synaptic activity unmasks dopamine D2 receptor modulation of a specific class of layer V pyramidal neurons in prefrontal cortex. J. Neurosci. *32*, 4959–4971.

Geisheker, M.R., Heymann, G., Wang, T., Coe, B.P., Turner, T.N., Stessman, H.A.F., Hoekzema, K., Kvarnung, M., Shaw, M., Friend, K., et al. (2017). Hotspots of missense mutation identify neurodevelopmental disorder genes and functional domains. Nat. Neurosci. *20*, 1043–1051.

Golden, C.E.M., Breen, M.S., Koro, L., Sonar, S., Niblo, K., Browne, A., Burlant, N., Di Marino, D., De Rubeis, S., Baxter, M.G., et al. (2019). Deletion of the KH1 Domain of Fmr1 Leads to Transcriptional Alterations and Attentional Deficits in Rats. Cereb. Cortex. *29*, 2228–2244.

Golding, N.L., Staff, N.P., and Spruston, N. (2002). Dendritic spikes as a mechanism for cooperative long-term potentiation. Nature *418*, 326–331.

Gong, B., Rhodes, K.J., Bekele-Arcuri, Z., and Trimmer, J.S. (1999). Type I and type II Na(+) channel alpha-subunit polypeptides exhibit distinct spatial and temporal patterning, and association with auxiliary subunits in rat brain. J. Comp. Neurol. *412*, 342–352.

Greer, P.L., Hanayama, R., Bloodgood, B.L., Mardinly, A.R., Lipton, D.M., Flavell, S.W., Kim, T.K., Griffith, E.C., Waldon, Z., Maehr, R., et al. (2010). The Angelman Syndrome protein Ube3A regulates synapse development by ubiquitinating arc. Cell *140*, 704–716.

Gulledge, A.T., and Stuart, G.J. (2003). Action potential initiation and propagation in layer 5 pyramidal neurons of the rat prefrontal cortex: absence of dopamine modulation. J. Neurosci. *23*, 11363–11372.

Hallermann, S., de Kock, C.P.J., Stuart, G.J., and Kole, M.H.P. (2012). State and location dependence of action potential metabolic cost in cortical pyramidal neurons. Nat. Neurosci. *15*, 1007–1014.

Hanse, E., Seth, H., and Riebe, I. (2013). AMPA-silent synapses in brain development and pathology. Nat. Rev. Neurosci. *14*, 839–850.

Hu, W., and Bean, B.P. (2018). Differential Control of Axonal and Somatic Resting Potential by Voltage-Dependent Conductances in Cortical Layer 5 Pyramidal Neurons. Neuron *97*, 1315–1326.e3.

Hu, W., Tian, C., Li, T., Yang, M., Hou, H., and Shu, Y. (2009). Distinct contributions of Na(v)1.6 and Na(v)1.2 in action potential initiation and backpropagation. Nat. Neurosci. *12*, 996–1002.

Johnson, K.W., Herold, K.F., Milner, T.A., Hemmings, H.C., Jr., and Platholi, J. (2017). Sodium channel subtypes are differentially localized to pre- and postsynaptic sites in rat hippocampus. J. Comp. Neurol. *525*, 3563–3578.

Kampa, B.M., Letzkus, J.J., and Stuart, G.J. (2006). Requirement of dendritic calcium spikes for induction of spike-timing-dependent synaptic plasticity. J. Physiol. *574*, 283–290.

Kampa, B.M., Letzkus, J.J., and Stuart, G.J. (2007). Dendritic mechanisms controlling spike-timing-dependent synaptic plasticity. Trends Neurosci. *30*, 456–463.

Kerchner, G.A., and Nicoll, R.A. (2008). Silent synapses and the emergence of a postsynaptic mechanism for LTP. Nat. Rev. Neurosci. *9*, 813–825.

Kim, Y., Hsu, C.L., Cembrowski, M.S., Mensh, B.D., and Spruston, N. (2015). Dendritic sodium spikes are required for long-term potentiation at distal synapses on hippocampal pyramidal neurons. eLife *4*.

Kole, M.H.P., and Stuart, G.J. (2012). Signal processing in the axon initial segment. Neuron *73*, 235–247.

Larkum, M.E., Zhu, J.J., and Sakmann, B. (1999a). A new cellular mechanism for coupling inputs arriving at different cortical layers. Nature *398*, 338–341.

Larkum, M.E., Kaiser, K.M., and Sakmann, B. (1999b). Calcium electrogenesis in distal apical dendrites of layer 5 pyramidal cells at a critical frequency of back-propagating action potentials. Proc. Natl. Acad. Sci. USA *96*, 14600–14604.

Li, T., Tian, C., Scalmani, P., Frassoni, C., Mantegazza, M., Wang, Y., Yang, M., Wu, S., and Shu, Y. (2014). Action potential initiation in neocortical inhibitory interneurons. PLoS Biol. *12*, e1001944.

Liao, Y., Deprez, L., Maljevic, S., Pitsch, J., Claes, L., Hristova, D., Jordanova, A., Ala-Mello, S., Bellan-Koch, A., Blazevic, D., et al. (2010). Molecular correlates of age-dependent seizures in an inherited neonatal-infantile epilepsy. Brain *133*, 1403–1414.

Lorincz, A., and Nusser, Z. (2008). Cell-type-dependent molecular composition of the axon initial segment. J. Neurosci. *28*, 14329–14340.

Lorincz, A., and Nusser, Z. (2010). Molecular Identity of Dendritic Voltage-Gated Sodium Channels. Science *328*, 906–909.

Magee, J.C., and Johnston, D. (1997). A synaptically controlled, associative signal for Hebbian plasticity in hippocampal neurons. Science *275*, 209–213.

Markram, H., Lübke, J., Frotscher, M., and Sakmann, B. (1997). Regulation of synaptic efficacy by coincidence of postsynaptic APs and EPSPs. Science *275*, 213–215.

Markram, H., Gerstner, W., and Sjöström, P.J. (2012). Spike-timing-dependent plasticity: a comprehensive overview. Front. Synaptic Neurosci. *4*, 2.

Meredith, R.M., and Mansvelder, H.D. (2010). STDP and Mental Retardation: Dysregulation of Dendritic Excitability in Fragile X Syndrome. Front. Synaptic Neurosci. *2*, 10.

Middleton, S.J., Kneller, E.M., Chen, S., Ogiwara, I., Montal, M., Yamakawa, K., and McHugh, T.J. (2018). Altered hippocampal replay is associated with memory impairment in mice heterozygous for the Scn2a gene. Nat. Neurosci. *21*, 996–1003.

Mishra, V., Karumuri, B.K., Gautier, N.M., Liu, R., Hutson, T.N., Vanhoof-Villalba, S.L., Vlachos, I., Iasemidis, L., and Glasscock, E. (2017). Scn2a deletion improves survival and brain-heart dynamics in the Kcna1-null mouse model of sudden unexpected death in epilepsy (SUDEP). Hum. Mol. Genet. *26*, 2091–2103.

Monteiro, P., and Feng, G. (2017). SHANK proteins: roles at the synapse and in autism spectrum disorder. Nat. Rev. Neurosci. *18*, 147–157.

Nestor, M.W., and Hoffman, D.A. (2012). Aberrant dendritic excitability: a common pathophysiology in CNS disorders affecting memory? Mol. Neurobiol. *45*, 478–487.

Ogiwara, I., Miyamoto, H., Morita, N., Atapour, N., Mazaki, E., Inoue, I., Takeuchi, T., Itohara, S., Yanagawa, Y., Obata, K., et al. (2007). Nav1.1 localizes to axons of parvalbumin-positive inhibitory interneurons: a circuit basis for epileptic seizures in mice carrying an Scn1a gene mutation. J. Neurosci. *27*, 5903–5914.

Ogiwara, I., Miyamoto, H., Tatsukawa, T., Yamagata, T., Nakayama, T., Atapour, N., Miura, E., Mazaki, E., Ernst, S.J., Cao, D., et al. (2018). Nav1.2 haplodeficiency in excitatory neurons causes absence-like seizures in mice. Commun. Biol. *1*, 96.

Pasciuto, E., Borrie, S.C., Kanellopoulos, A.K., Santos, A.R., Cappuyns, E., D'Andrea, L., Pacini, L., and Bagni, C. (2015). Autism Spectrum Disorders: Translating human deficits into mouse behavior. Neurobiol. Learn. Mem. *124*, 71–87.

Pernía-Andrade, A.J., Goswami, S.P., Stickler, Y., Fröbe, U., Schlögl, A., and Jonas, P. (2012). A deconvolution-based method with high sensitivity and temporal resolution for detection of spontaneous synaptic currents in vitro and in vivo. Biophys. J. *103*, 1429–1439.

Planells-Cases, R., Caprini, M., Zhang, J., Rockenstein, E.M., Rivera, R.R., Murre, C., Masliah, E., and Montal, M. (2000). Neuronal death and perinatal lethality in voltage-gated sodium channel α(II)-deficient mice. Biophys. J. *78*, 2878–2891.

Sala, C., Futai, K., Yamamoto, K., Worley, P.F., Hayashi, Y., and Sheng, M. (2003). Inhibition of dendritic spine morphogenesis and synaptic transmission by activity-inducible protein Homer1a. J. Neurosci. *23*, 6327–6337.

Sanders, S.J. (2015). First glimpses of the neurobiology of autism spectrum disorder. Curr. Opin. Genet. Dev. *33*, 80–92.

Sanders, S.J., Murtha, M.T., Gupta, A.R., Murdoch, J.D., Raubeson, M.J., Willsey, A.J., Ercan-Sencicek, A.G., DiLullo, N.M., Parikshak, N.N., Stein, J.L., et al. (2012). De novo mutations revealed by whole-exome sequencing are strongly associated with autism. Nature *485*, 237–241.

Sanders, S.J., He, X., Willsey, A.J., Ercan-Sencicek, A.G., Samocha, K.E., Cicek, A.E., Murtha, M.T., Bal, V.H., Bishop, S.L., Dong, S., et al.; Autism Sequencing Consortium (2015). Insights into Autism Spectrum Disorder Genomic Architecture and Biology from 71 Risk Loci. Neuron *87*, 1215–1233.

Sanders, S.J., Campbell, A.J., Cottrell, J.R., Moller, R.S., Wagner, F.F., Auldridge, A.L., Bernier, R.A., Catterall, W.A., Chung, W.K., Empfield, J.R., et al. (2018). Progress in Understanding and Treating SCN2A -Mediated Disorders. Trends Neurosci. *41*, 442–456.

Satterstrom, F.K., Kosmicki, J.A., Wang, J., Breen, M.S., De Rubeis, S., An, J.Y., Peng, M., Collins, R.L., Grove, J., Klei, L., et al. (2018). Novel genes for autism implicate both excitatory and inhibitory cell lineages in risk. bioRxiv. https://doi.org/10.1101/484113.

Shen, H.W., Gipson, C.D., Huits, M., and Kalivas, P.W. (2014). Prelimbic cortex and ventral tegmental area modulate synaptic plasticity differentially in nucleus accumbens during cocaine-reinstated drug seeking. Neuropsychopharmacology *39*, 1169–1177.

Short, S.M., Oikonomou, K.D., Zhou, W.L., Acker, C.D., Popovic, M.A., Zecevic, D., and Antic, S.D. (2017). The stochastic nature of action potential backpropagation in apical tuft dendrites. J. Neurophysiol. *118*, 1394–1414.

Silverman, J.L., Yang, M., Lord, C., and Crawley, J.N. (2010). Behavioural phenotyping assays for mouse models of autism. Nat. Rev. Neurosci. *11*, 490–502.

Spencer, C.M., Alekseyenko, O., Hamilton, S.M., Thomas, A.M., Serysheva, E., Yuva-Paylor, L.A., and Paylor, R. (2011). Modifying behavioral phenotypes in Fmr1KO mice: genetic background differences reveal autistic-like responses. Autism Res. *4*, 40–56.

Stuart, G.J., and Häusser, M. (2001). Dendritic coincidence detection of EPSPs and action potentials. Nat. Neurosci. *4*, 63–71.

Stuart, G., Schiller, J., and Sakmann, B. (1997). Action potential initiation and propagation in rat neocortical pyramidal neurons. J. Physiol. *505*, 617–632.

Sugathan, A., Biagioli, M., Golzio, C., Erdin, S., Blumenthal, I., Manavalan, P., Ragavendran, A., Brand, H., Lucente, D., Miles, J., et al. (2014). *CHD8* regulates neurodevelopmental pathways associated with autism spectrum disorder in neural progenitors. Proc. Natl. Acad. Sci. USA *111*, E4468–E4477.

Taddese, A., and Bean, B.P. (2002). Subthreshold sodium current from rapidly inactivating sodium channels drives spontaneous firing of tuberomammillary neurons. Neuron *33*, 587–600.

Tai, C., Abe, Y., Westenbroek, R.E., Scheuer, T., and Catterall, W.A. (2014). Impaired excitability of somatostatin- and parvalbumin-expressing cortical interneurons in a mouse model of Dravet syndrome. Proc. Natl. Acad. Sci. USA *111*, E3139–E3148.

Tatsukawa, T., Raveau, M., Ogiwara, I., Hattori, S., Miyamoto, H., Mazaki, E., Itohara, S., Miyakawa, T., Montal, M., and Yamakawa, K. (2019). *Scn2a* haploinsufficient mice display a spectrum of phenotypes affecting anxiety, sociability, memory flexibility and ampakine CX516 rescues their hyperactivity. Mol. Autism *10*, 15.

Tsai, N.P., Wilkerson, J.R., Guo, W., Maksimova, M.A., DeMartino, G.N., Cowan, C.W., and Huber, K.M. (2012). Multiple autism-linked genes mediate synapse elimination via proteasomal degradation of a synaptic scaffold PSD-95. Cell *151*, 1581–1594.

Tzounopoulos, T., Kim, Y., Oertel, D., and Trussell, L.O. (2004). Cell-specific, spike timing-dependent plasticities in the dorsal cochlear nucleus. Nat. Neurosci. *7*, 719–725.

Williams, S.R., and Mitchell, S.J. (2008). Direct measurement of somatic voltage clamp errors in central neurons. Nat. Neurosci. *11*, 790–798.

Williams, M.R., DeSpenza, T., Jr., Li, M., Gulledge, A.T., and Luikart, B.W. (2015). Hyperactivity of newborn Pten knock-out neurons results from increased excitatory synaptic drive. J. Neurosci. *35*, 943–959.

Willsey, A.J., Sanders, S.J., Li, M., Dong, S., Tebbenkamp, A.T., Muhle, R.A., Reilly, S.K., Lin, L., Fertuzinhos, S., Miller, J.A., et al. (2013). Coexpression networks implicate human midfetal deep cortical projection neurons in the pathogenesis of autism. Cell *155*, 997–1007.

Wolff, M., Johannesen, K.M., Hedrich, U.B.S., Masnada, S., Rubboli, G., Gardella, E., Lesca, G., Ville, D., Milh, M., Villard, L., et al. (2017). Genetic and phenotypic heterogeneity suggest therapeutic implications in SCN2A-related disorders. Brain *140*, 1316–1336.

Workman, A.D., Charvet, C.J., Clancy, B., Darlington, R.B., and Finlay, B.L. (2013). Modeling transformations of neurodevelopmental sequences across mammalian species. J. Neurosci. *33*, 7368–7383.

Xu, B., Zang, K., Ruff, N.L., Zhang, Y.A., McConnell, S.K., Stryker, M.P., and Reichardt, L.F. (2000). Cortical degeneration in the absence of neurotrophin signaling: dendritic retraction and neuronal loss after removal of the receptor TrkB. Neuron *26*, 233–245.

Xu, N.L., Harnett, M.T., Williams, S.R., Huber, D., O'Connor, D.H., Svoboda, K., and Magee, J.C. (2012). Nonlinear dendritic integration of sensory and motor input during an active sensing task. Nature *492*, 247–251.

Yamagata, T., Ogiwara, I., Mazaki, E., Yanagawa, Y., and Yamakawa, K. (2017). Nav1.2 is expressed in caudal ganglionic eminence-derived disinhibitory interneurons: Mutually exclusive distributions of Nav1.1 and Nav1.2. Biochem. Biophys. Res. Commun. *491*, 1070–1076.

Yashiro, K., Riday, T.T., Condon, K.H., Roberts, A.C., Bernardo, D.R., Prakash, R., Weinberg, R.J., Ehlers, M.D., and Philpot, B.D. (2009). Ube3a is required for experience-dependent maturation of the neocortex. Nat. Neurosci. *12*, 777–783.

Yasuda, R., Nimchinsky, E.A., Scheuss, V., Pologruto, T.A., Oertner, T.G., Sabatini, B.L., and Svoboda, K. (2004). Imaging calcium concentration dynamics in small neuronal compartments. Sci. STKE *2004*, pl5–pl5.

Yi, F., Danko, T., Botelho, S.C., Patzke, C., Pak, C., Wernig, M., and Südhof, T.C. (2016). Autism-associated SHANK3 haploinsufficiency causes Ih channelopathy in human neurons. Science *352*, aaf2669.

STAR★METHODS

KEY RESOURCES TABLE

REAGENT or RESOURCE	SOURCE	IDENTIFIER
Bacterial and Virus Strains		
AAV5-Ef1α-Cre-mCherry	UNC Viral Core	N/A
Chemicals, Peptides, and Recombinant Proteins		
NBQX disodium salt	Tocris	0373
Tetrodotoxin-citrate	Alomone	T-550
(*R*)-CPP	Tocris	0247
Picrotoxin	Tocris	1128
Fluo-5F, Pentapotassium Salt, cell impermeant	Invitrogen	F14221
Alexa Fluor 594 hydrazide	Invitrogen	A10438
Prolong Gold Antifade with DAPI	Life Technologies	P36941
Experimental Models: Organisms/Strains		
Mouse: Ai14: 6;129S6-*Gt(ROSA)26Sor*$^{tm14(CAG-tdTomato)Hze}$/J	The Jackson Laboratory	JAX: 007908
Mouse: C57B6J	The Jackson Laboratory	JAX: 000664
Mouse: B6.Cg-Tg(Camk2a-cre)T29-1Stl/J	The Jackson Laboratory	JAX:005359
Mouse: *Scn2a*$^{+/-}$	M. Montal / E. Glasscock	PMID: 10827969, 28334922
Mouse: *Scn2a*$^{+/fl}$	This study	N/A
Software and Algorithms		
IGOR Pro	Wavemetrics	RRID:SCR_000325; v6.3
FIJI	https://fiji.sc/	RRID:SCR_002285
MATLAB	Mathworks	RRID:SCR_001622; v2016a
Python	https://www.python.org	RRID:SCR_008394 ; v3.5.2
IMARIS	Bitplane	RRID:SCR_007370; v6.3
Prism	Graphpad	RRID:SCR_002798; v8
Statview	SAS	v5.0.1
Ethovision	Noldus	RRID:SCR_000441

LEAD CONTACT AND MATERIALS AVAILABILITY

Requests for reagents and resources should be directed to the Lead Contact, Kevin Bender (kevin.bender@ucsf.edu).

EXPERIMENTAL MODEL AND SUBJECT DETAILS

All experimental procedures were performed in accordance with UCSF and Gladstone Institutes IACUC guidelines. All experiments were performed on mice housed under standard conditions with *ad libitum* access to food and water. C57B6J (JAX: 000664), B6.Cg-Tg(Camk2a-cre)T29-1Stl/J (Jax: 005359), Ai14: 6;129S6-Gt(ROSA)26Sortm14(CAG-tdTomato)Hze/J (JAX: 007908) were obtained from The Jackson Laboratory and bred in our onsite colony. *Scn2a*$^{+/-}$ mice were provided by Drs. E. Glasscock and M. Montal (Mishra et al., 2017; Planells-Cases et al., 2000). *Scn2a*$^{+/fl}$ mice were created by inserting LoxP sites around exon 2 of the *Scn2a* gene (Fig, S6A, Cyagen). A targeting vector was generated by PCR using BAC clone RP23-332C13 and RP24-42717 from the C57BL/6J library to create homology arms around a LoxP flanked cKO region that includes exon 2 of the *Scn2a* gene. The targeting vector included a Neo cassette flanked by Rox sites for positive selection, and DTA outside of the homology arms for negative selection. The linearized vector was subsequently delivered to ES cells (C57BL/6) via electroporation, followed by drug selection, PCR screening, and Southern Blot confirmation. Confirmed clones were then introduced into host embryos and transferred to surrogate mothers. Chimerism in the resulting pups was identified via coat color. F0 male chimeras were bred with C57BL/6 females to generate F1 heterozygous mutants that were identified by PCR.

METHOD DETAILS

Ex Vivo Electrophysiology

Mice aged P4 through P62 were anesthetized, and 250 μm-thick coronal slices containing medial prefrontal cortex, medial orbitofrontal cortex, hippocampal CA1, or primary visual cortex (Figure S3A) were prepared. Slices were prepared from *Scn2a*$^{+/-}$, CaMKII-Cre (MGI: 2446639)::*Scn2a*$^{+/fl}$, Parv-Cre (MGI: 3590684)::Ai14::*Scn2a*$^{+/-}$, SOM-Cre (MGI: 4838416)::Ai14::*Scn2a*$^{+/-}$, or *Scn2a* wild-type littermates (genotyped by PCR). All data were acquired and analyzed blind to *Scn2a* genotype, except for experiments examining the effects of tetrodotoxin in a wild-type background (AP waveform and synaptic plasticity), and the effects of sparse Cre transfection in *Scn2a*$^{+/fl}$ mice. Data were acquired from both sexes (blind to sex), with no sex-dependent differences noted in measurements made in acute slice recordings [e.g., AMPA:NMDA ratio, combined data across constitutive and conditional heterozygote cases: Male +/+ 5.1 ± 0.3, n = 8, Female +/+: 4.7 ± 0.3, n = 22, Male ± : 2.4 ± 0.3, = 18, Female ± : 3.1 ± 0.3, n = 11; p = 0.13, 2-factor ANOVA. Peak rising dV/dt of AP, combined data from P23-62 constitutive and > P50 conditional heterozygote cases: Male +/+: 584.4 ± 8.8 V/s, n = 48; Female +/+: 588.0 ± 22.8, n = 6; Male ± : 405.3 ± 8.1, n = 32; Female ± : 449 ± 19.0, n = 9; p = 0.21, 2-factor ANOVA). Cutting solution contained (in mM): 87 NaCl, 25 $NaHCO_3$, 25 glucose, 75 sucrose, 2.5 KCl, 1.25 NaH_2PO_4, 0.5 $CaCl_2$ and 7 $MgCl_2$; bubbled with 5%CO_2/95%O_2; 4°C. Following cutting, slices were either incubated in the same solution or in the recording solution for 30 min at 33°C, then at room temperature until recording. Recording solution contained (in mM): 125 NaCl, 2.5 KCl, 2 $CaCl_2$, 1 $MgCl_2$, 25 $NaHCO_3$, 1.25 NaH_2PO_4, 25 glucose; bubbled with 5%CO_2/95%O_2; 32-34°C, ~310 mOsm.

Neurons were visualized with differential interference contrast (DIC) optics for conventional visually guided whole-cell recording, or with 2-photon-guided imaging of reporter-driven tdTomato fluorescence overlaid on an image of the slice (scanning DIC). For current-clamp recordings and voltage-clamp recordings of K^+ currents, patch electrodes (Schott 8250 glass, 3-4 MΩ tip resistance) were filled with a solution containing (in mM): 113 K-Gluconate, 9 HEPES, 4.5 $MgCl_2$, 0.1 EGTA, 14 $Tris_2$-phosphocreatine, 4 Na_2-ATP, 0.3 tris-GTP; ~290 mOsm, pH: 7.2-7.25. For Ca^{2+} imaging, EGTA was replaced with 250 μM Fluo-5F and 20 μM Alexa 594. For voltage-clamp recordings of persistent Na^+ currents and synaptic activity, internal solution contained (in mM): 110 $CsMeSO_3$, 40 HEPES, 1 KCl, 4 NaCl, 4 Mg-ATP, 10 Na-phosphocreatine, 0.4 Na_2-GTP, 0.1 EGTA; ~290 mOsm, pH: 7.22. All data were corrected for measured junction potentials of 12 and 11 mV in K- and Cs-based internals, respectively.

Electrophysiological data were acquired using Multiclamp 700A or 700B amplifiers (Molecular Devices) via custom routines in IgorPro (Wavemetrics). For measurements of action potential waveform, data were acquired at 50 kHz and filtered at 20 kHz. For all other measurements, data were acquired at 10-20 kHz and filtered at 3-10 kHz. For current-clamp recordings, pipette capacitance was compensated by 50% of the fast capacitance measured under gigaohm seal conditions in voltage-clamp prior to establishing a whole-cell configuration, and the bridge was balanced. For voltage-clamp recordings, pipette capacitance was compensated completely, and series resistance was compensated 50%. Series resistance was < 15 MΩ in all recordings. Experiments were omitted if input resistance changed by > ± 15%.

Between P4 and P10, whole-cell current-clamp recordings were made from in the center of the cortical plate, corresponding to developing layer 5 (Cánovas et al., 2015). Putative pyramidal cells were identified based on regular spiking characteristics. Pyramidal cell identity was validated by 2-photon visualization of dendritic spines in a subset of these recordings (25/81). After P13, laminae became more distinct and recordings were restricted to L5b. In pyramidal cells aged > P17, AP characteristics are known to vary based cell class (Clarkson et al., 2017; Dembrow et al., 2010). To minimize variability, recordings were restricted to cells with low or high HCN expression levels, corresponding to intratelencephalic (IT) or pyramidal tract (PT) neurons, respectively. In current clamp, PT neurons were defined as those that exhibited a voltage rebound more depolarized that V_{rest} following a strong hyperpolarizing current (−400 pA, 120 ms) that peaked within 90 ms of current offset (Clarkson et al., 2017). All others were defined as IT. These metrics were not employed in cells from < P15 due to a lack of mature HCN-mediated current. AP threshold and peak dV/dt measurements were determined from the first AP evoked by a near-rheobase current in pyramidal cells (300 ms duration; 10 pA increments), or the first AP within a train of APs with a minimum inter-AP frequency of 25 Hz in inhibitory neurons. Threshold was defined as the V_m when dV/dt measurements first exceeded 15 V/s.

Miniature excitatory and inhibitory postsynaptic currents (mEPSC, mIPSC) were assessed in the presence of 10 μM R-CPP and 400 nM TTX. mEPSCs and mIPSCs were measured while voltage-clamping neurons at −80 and 0 mV, respectively. Events were detected using a deconvolution algorithm based on Pernía-Andrade et al. (2012), with a noise threshold of 3.5x. All events larger than ± 2 pA that were separated by 1 ms were analyzed and subsequently screened manually. Baseline recording noise was not different across genotype (P27 mEPSC root mean square noise, WT: 2.1 ± 0.2 pA, n = 23; *Scn2a*$^{+/-}$: 2.2 ± 0.2 pA, n = 19, p = 0.6, Mann-Whitney test).

In experiments measuring paired pulse ratio and AMPA:NMDA ratio, EPSCs were evoked via a bipolar glass theta electrode placed ~200 μm lateral to the recorded neuron in layer 5. Paired pulse ratio was assessed in the presence of 10 μM R-CPP and 25 μM picrotoxin at −80 mV. Overall divalent concentration was maintained when calcium was lowered from 2 to 1 mM by increasing $MgCl_2$ from 1 to 2 mM. For AMPA:NMDA ratio, R-CPP was omitted and neurons were held at −80 and +30 mV to assess AMPA and NMDA-mediated components. AMPA and NMDA components were defined as the peak inward current at −80 mV and the outward current 50 ms after stimulus onset at +30 mV, respectively.

For sparse Cre expression experiments, mice were anesthetized with isoflurane and positioned in a stereotaxic apparatus. 500 nL volumes of AAV-EF1A-Cre-IRES-mCherry (UNC Vector Core) diluted with saline (1:10) were injected into the mPFC of *Scn2a*$^{fl/+}$ mice (stereotaxic coordinates [mm]: anterior-posterior [AP], +1.7, mediolateral [ML] −0.35; dorsoventral [DV]: −2.6). Mice were used in experiments four weeks post injection.

Persistent Na^+ and currents were activated with 500 ms voltage steps from −90 mV and corrected using p/n leak subtraction. 10-15 trials were averaged per voltage step. Current amplitudes were calculated as the average of the last 100 ms of each step. Experiments were performed in 25 μM picrotoxin, 10 μM NBQX, 10 mM TEA, 2 mM 4-AP, 200 μM Cd^{2+}, 2 μM TTA-P2, and 1 mM Cs^+. K^+ currents were activated with 500 ms voltage steps from −90 to −20, in 10 mV increments. 5 trials were averaged per voltage step. Current amplitudes were calculated from the transient peak and sustained components (last 50 ms). Experiments were performed in 500 nM TTX, 25 μM picrotoxin, 10 μM NBQX, and 1 mM Cs^+. Ca^{2+} channels were not blocked to allow for activation of Ca^{2+}-dependent K^+ channels.

In burst-based spike timing-dependent plasticity protocols, excitatory postsynaptic potentials (EPSPs) were evoked with a theta stimulating electrode placed in layer 1, 25-50 μm from the L1/2 border, 350-500 μm dorsal to the recorded L5b pyramidal cell. After establishing a stable baseline (EPSP ISI: 0.1 Hz), EPSPs were paired with AP bursts evoked by 500-800 pA somatic current steps (20 ms, onset: 10 ms after EPSP stimulation, 2 APs at > 100 Hz). These EPSP-AP pairings were delivered in a train of 5 at 100 ms ISI. Trains were repeated every 5 s for 20 trials. Following induction, EPSP stimulation frequency was reset to 0.1 Hz, and changes in EPSP slope were assessed by comparing data 15-25 min following induction to baseline. For experiments performed in 5 nM TTX, bursts were evoked with somatic current injection steps of larger amplitude (800-1500 pA).

Two-Photon Imaging

Two-photon laser scanning microscopy (2PLSM) was performed as previously described (Bender and Trussell, 2009). A 2-photon source (Coherent Ultra II) was tuned to 810 nm for morphology and calcium imaging. Epi- and transfluorescence signals were captured either through a 40 × , 0.8 NA objective for calcium imaging or a 60 × , 1.0 NA objective for spine morphology imaging, paired with a 1.4 NA oil immersion condenser (Olympus). Fluorescence was split into red and green channels using dichroic mirrors and band-pass filters (575 DCXR, ET525/70 m-2p, ET620/60 m-2p, Chroma). Green fluorescence (Fluo-5F) was captured with 10770-40 photomultiplier tubes selected for high quantum efficiency and low dark counts (PMTs, Hamamatsu). Red fluorescence (Alexa 594) was captured with R9110 PMTs. Data were collected in linescan mode (2–2.4 ms/line, including mirror flyback). For calcium imaging, data were presented as averages of 10-20 events per site, and expressed as $\Delta(G/R)/(G/R)_{max}*100$, where $(G/R)_{max}$ was the maximal fluorescence in saturating Ca^{2+} (2 mM) (Yasuda et al., 2004). Backpropagation experiments were performed in 25 μM picrotoxin, 10 μM NBQX and 10 μM R-CPP.

Spine morphology and density images were obtained during 2PLSM images obtained at 2x the Nyquist resolution limit for 810 nm excitation, with z stacks through the dendritic arbor (0.1 μm steps in the z axis). For constitutive knockout animals, z stacks of dendritic spines were acquired developing (P5-6) and mature (P24-36) neurons from secondary or tertiary dendritic branches in the apical tuft (Mean distance from soma: P24-36 WT = 350 ± 52 μm, P24-36 *Scn2a*$^{+/-}$ = 308 ± 37 μm, P5-6 WT = 197 ± 39 μm, P24-36 *Scn2a*$^{+/-}$ = 197 ± 68 μm) and primary and secondary basal dendritic branches (Mean distance P24-36 WT = 99 ± 23 μm, P24-36 *Scn2a*$^{+/-}$ = 106 ± 25 μm). For conditional knockout animals, z stacks were acquired from P75-76 *Scn2a*$^{fl/+}$::CaMKII-Cre mice and littermate controls from secondary or tertiary dendritic branches in the apical tuft (WT = 390 ± 51 μm, *Scn2a*$^{fl/+}$::CaMKII-cre = 401 ± 30 μm) and primary and secondary basal dendritic branches (WT = 98 ± 23 μm, *Scn2a*$^{fl/+}$::CaMKII-Cre = 86 ± 25 μm). Stacks were post-processed with the CANDLE denoising protocol (Coupé et al., 2012), then reconstructed using IMARIS 6 (Bitplane). Maximum intensity image projections are displayed within the main and supplemental figures using the "Red Hot" lookup table (FIJI). Full dendritic reconstructions were stitched together using pairwise stitching in FIJI before generation of maximum intensity projection.

Behavioral Analyses

Three separate cohorts of mice were assessed, blind to genotype. In the first, tests included open field, elevated plus maze, balance beam, rotarod, nesting, spontaneous alternation, grooming, response and reversal learning, and three trial social interactions. Based on results of this screen, four trial social preference was assessed in a second cohort and response and reversal learning was assessed in the second and third cohort. Open field and elevated plus maze were also reassessed in each cohort to determine whether each cohort responded similarly in these anxiety-related assays. Open Field – Mice were transferred to the testing room 60 minutes prior to the start of testing. Mice were then placed in a clear plastic chamber (41 × 41 × 30 cm) and allowed to explore. Movement in the center and outer periphery were recorded by an array of 16 × 16 photobeams (San Diego Instruments).

Elevated Plus Maze

Mice were placed at the center of an elevated plus maze consisting of two open arms (5.715 cm wide, 70.485 cm long), and two enclosed arms (5.715 cm wide, 70.485 cm long, 16.51cm walls) elevated 63 cm above the ground and were allowed to explore for 10 minutes. Location, distance traveled, and arm entries were measured by infrared photobeam breaks.

Balance Beam

On day 1, mice were first trained to talk across a wide beam (37 cm long x 15.875 mm diameter circular beam) over two guided trials. Following training, mice completed three trials (15-minute inter-trial interval) where they were placed end of the beam and traversed

the wide beam unguided into an opposing dark chamber. On day 2 the mice completed three trials using a medium beam (37 cm x 12.7 mm diameter circular beam), and on day 3 three trials were completed on the small beam (37 cm x 6.35 mm wide square beam). For each tested trial, the latency to traverse, number of foot slips, and falls were recorded. All testing was performed under normal light conditions.

Rotarod

Mice were trained on a rotarod apparatus over three trials (inter-trial interval 15 minutes) with the rod rotating at a constant speed of 16 rotations per minute (RPM). Following training, mice were tested on 2 consecutive days with 2 sessions of 3 trials each (2-hour inter-session interval, 15-minute inter-trial interval) in which mice were placed on a rotarod apparatus that gradually accelerated from 4 RPM to 40 RPM in 4 rpm increments every 30 s. Trials would end when the mouse would fall off the apparatus or after 5 minutes. All testing was performed under normal light conditions.

Nesting

Mice were placed in a standard mouse cage with 2 cm of paper chip bedding and a single nestlet (5 cm square of pressed cotton batting). Nests in the cage were then scored 2, 6, and 24 hours after the introduction of the mouse on the following scale: 0 = nestlet untouched, 1 = less than 10% of the nestlet is shredded, 2 = 10%–50% of the nestlet is shredded but there is no shape to the nest, 3 = 10%–50% of the nestlet is shredded and there is shape to the nest, 4 = 50%–90% of the nestlet is shredded but there is no shape to the nest, 5 = 50%–90% of the nestlet is shredded and there is shape to the nest, 6 = Over 90% of the nestlet is shredded but the nest is flat, 7 = Over 90% of the nestlet is shredded and the nest has walls that are as tall as the mouse on at least 50% of its sides. Half scores were given to nests that lacked well-defined walls but had clear indentations in the middle where the mouse could sit.

Spontaneous Alternation

Mice were placed in an arm of a Y-maze consisting of three arms (30 × 5.5 × 15 cm) and allowed to explore for 6 minutes. Successful alterations were counted when the mouse entered all three arms in succession without repeating an arm. Percent alternation was calculated by the total number of alterations in 6 minutes/(total number of entries - 2) * 100. Entries were defined as all four paws entering an arm.

Grooming

Mice were placed in a clear plastic container and left undisturbed for 20 minutes. Following 10 minutes of habituation, the number of grooming bouts and the total time spent grooming during the subsequent 10-minute period were then manually scored.

Response and Reversal Learning

Mice were singly housed and habituated to the testing room for two days prior to the start of testing. Under red light conditions, mice were placed in the start of a water T-maze (10 cm wide, 31 cm long and 17 cm tall) and were required to locate a submerged escape platform at the end of either the right of left arm of the T-maze. Mice performed 4 trials per day in 2 sessions of 2 trials each (3-hour inter-session interval and 15 minute inter-trial interval) for four consecutive days. The platform location remained in the same location across trials for each mouse, and platform location was counterbalanced between mice. On day 5, the platform location was moved to the opposite arm and mice were required to learn the new platform location. Mice performed 6 trials a day in 2 separate sessions of 3 trials (3-hour inter-session interval and 15 minute inter-trial interval) for 4 consecutive days. The maximum length of each trial was 60 s, and if mice failed to find the platform within the time limit they were guided to the platform. After successfully finding the platform, the mice were allowed to remain for 10 s. Trials were considered incorrect if the mouse entered failed to enter the correct arm first or if the trial time limit expired. All trials were recorded and tracked using Ethovision (Noldus).

Social Approach

Testing was conducted with a white acrylic box divided into two chambers with clear acrylic dividers containing arch-shaped entrances at their center (24in. long, divided into two 12 in chambers, 16 in. wide, and 8.75 in. tall). The chambers contained 10cm square, open-bottomed social enclosures made of clear acrylic with two staggered rows of small access holes (0.5cm in diameter) 2.5cm from the bottom on the 2 sides of the enclosures facing toward the center of the chamber. On day one, mice were first habituated to the empty testing apparatus in 3 10-minute sessions (Mice were returned to their home cage for at least 10 minutes between sessions). On day 2, mice were allowed to explore the empty apparatus for a fourth habituation trial. Social approach was then assessed in a fifth trial by placing a stimulus mouse in one of the two enclosures and the test mouse was allowed to explore either the empty or social enclosures for 10 minutes. Each trial was recorded by video and analyzed with Ethovision. Interaction time was considered the total time spent sniffing within 2 cm of the social enclosures.

Four Trial Social Preference

Sex-matched stimulus mice were habituated to the enclosures for 3 10-minute sessions, between which they were returned to their home cages for at least 10 minutes. Both the experimental and stimulus mice were brought into testing room and given one hour to acclimate to the normal lighting conditions and room prior to testing. For trial 1, the stimulus and toy mouse (Hexbug 480-4466, white) were placed in the enclosures, after which the experimental mouse was placed in the chamber and given 10 minutes to freely explore the box and interact with the social enclosures. The stimulus and experimental mouse were then returned to their home cages for 1 hour before starting trial 2. Trial 2 and 3 proceeded identically to trial 1, using the same stimulus mouse in the same social enclosure. Trial 4 proceeded as in trials 1-3, however the toy mouse was replaced with a novel sex-matched stimulus mouse. For three trial social interaction, only trials 1-3 were assessed. Social preference was assessed on trial 4. Each trial was recorded by video and analyzed with Ethovision. Interaction time was considered the total time spent sniffing within 2 cm of the social enclosures.

Modeling

A pyramidal cell compartmental model was implemented in the NEURON environment (v7.5), with baseline distributions of $Na_V1.2$ and $Na_V1.6$ set as previously described (Ben-Shalom et al., 2017), based on a pyramidal cell model by Hallermann et al. (2012). For phase plane comparisons, the first AP evoked with 2.2 nA stimulus intensity (100 ms duration) were compared in each model configuration. For backpropagation into dendritic arbors, stimuli were shorted to 20 ms to match empirical stimulus conditions (STDP). Stimulus intensity was increased to 2.7 nA. Relative distributions of $Na_V1.2$ and $Na_V1.6$ in the proximal AIS, soma and dendrite were adjusted as described in figure legends. AP waveforms were assessed at 5 locations along the apical dendrite, and AP amplitude was defined as the difference between AP peak V_m and AP threshold (when voltage first exceeds 15 V/s).

Chemicals

Fluo-5F pentapotassium salt, and Alexa Fluor 594 hydrazide Na^+ salt were from Invitrogen. Picrotoxin, R-CPP, and NBQX were from Tocris. TTX-citrate was from Alomone. All others were from Sigma.

QUANTIFICATION AND STATISTICAL ANALYSIS

Data are summarized either as single points with error bars (mean ± standard error) or with boxplots depicting the median, quartiles, and 90% tails with individual datapoints overlaid. n denotes cells for all electrophysiology, spines for spine morphology, and animals for behavior. Data were obtained from 2-9 mice per condition for electrophysiology and imaging experiments. Behavioral cohorts were randomized and the experimentalist was blind to genotype. For electrophysiology and imaging experiments, acute slices were typically prepared from WT and conditional or constitutive *Scn2a*$^{+/-}$ littermates simultaneously (genotype blind to experimentalists), with experiments interleaved between the two genotypes to control for recording conditions. Group sample sizes were chosen based on standards in the field, and no statistical methods were used to predetermine sample size. Unless specifically noted, no assumptions were made about the underlying distributions of the data and two-sided, rank-based nonparametric tests were used. Statistical tests are noted throughout text. Significance was set at an alpha value of 0.05, with a Bonferroni correction for multiple comparisons when appropriate. Statistical analysis was performed using Prism 8 (Graphpad Software), Statview (SAS), and custom routines in MATLAB R2016b (Mathworks), Python 3.6.4 and R 3.4.3.

Neuron, Volume *103*

Supplemental Information

The Autism-Associated Gene *Scn2a* Contributes to Dendritic Excitability and Synaptic Function in the Prefrontal Cortex

Perry W.E. Spratt, Roy Ben-Shalom, Caroline M. Keeshen, Kenneth J. Burke Jr., Rebecca L. Clarkson, Stephan J. Sanders, and Kevin J. Bender

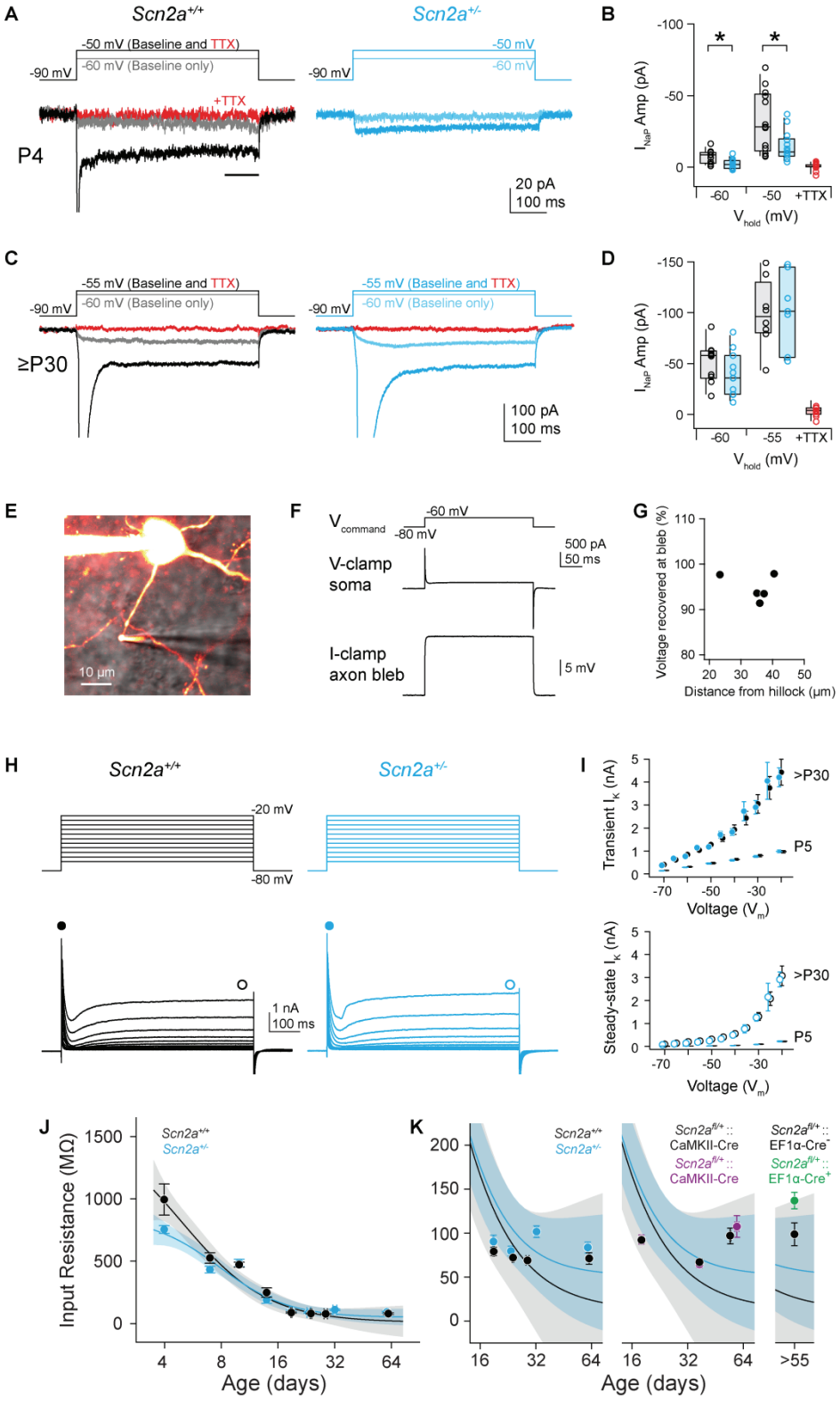

Supplemental Figure 1: Additional electrophysiological measurements in *Scn2a*$^{+/-}$ neurons (Related to Figure 1)

A: At P4, Na_V-mediated currents were evoked with voltage steps from -90 mV to either -60 or -50 mV. Note generation of transient current at -50 mV. Data are color coded to match voltage step.

Currents generated in TTX were assessed with steps from -90 to -50 mV only. Horizontal black bar highlights timing of persistent currents measurement.

B: Summary of persistent current amplitudes. Open circles are single cells. Box plots are median, quartiles, and 90% tails. TTX was applied in a subset of cells, and data were pooled over both *Scn2a*$^{+/+}$ and *Scn2a*$^{+/-}$ cells. *: $p < 0.05$, Mann-Whitney.

C: Na_V-mediated currents from P30-40 neurons. Note that voltage steps range from -90 to either -60 or -55, instead of -50, due to increased current amplitude and voltage-dependent differences between $Na_V1.2$ presumably recruited in P4 neurons and $Na_V1.6$ presumably recruited in P3-40 neurons.

D: Summary as in *b*, but for P30-40 neurons. No differences observed between *Scn2a*$^{+/+}$ and *Scn2a*$^{+/-}$ cells at this age range.

E: 2PLSM fluorescence image overlaid with scanning-DIC of slice, showing simultaneous recording from soma and axon bleb. Bleb electrode filled with dye-free solution.

F: Example of voltage command delivered via somatic pipette and resultant voltages recorded in current clamp in axon bleb.

G: Percent of somatic voltage recovered via axon pipette vs. axonal length from hillock. Circles are single recordings.

H: Potassium currents generated from voltage steps from -90 to -20 mV (10 mV increments for >P32-39 cells, 20 mV increments for P5 cells) in *Scn2a*$^{+/+}$ and *Scn2a*$^{+/-}$ cells. Closed and open circles denote when transient and steady-state current amplitudes were analyzed. n = 6 cells per condition.

I: Summary of current amplitudes per voltage step. Circles and bars are mean ± SEM. No differences noted across genotype.

J: Left: Development of input resistance in *Scn2a*$^{+/+}$ and *Scn2a*$^{+/-}$ cells. Data fit with a generalized logistic function with 95% confidence bands based on group mean values. Circles and bars are mean ± SEM within an age group.

K: Left: same data as in J, but restricted to P16-64 with an expanded Y axis to better visualize data at these ages. Middle: development of action potential amplitude of *Scn2a*$^{fl/+}$::CaMKII-cre and WT mice. Right: Action potential amplitude of Cre+ and Cre- *Scn2a*$^{fl/+}$ neurons sparsely infected with AAV,-EF1α-Cre-mCherry at P28. No statistical differences noted.

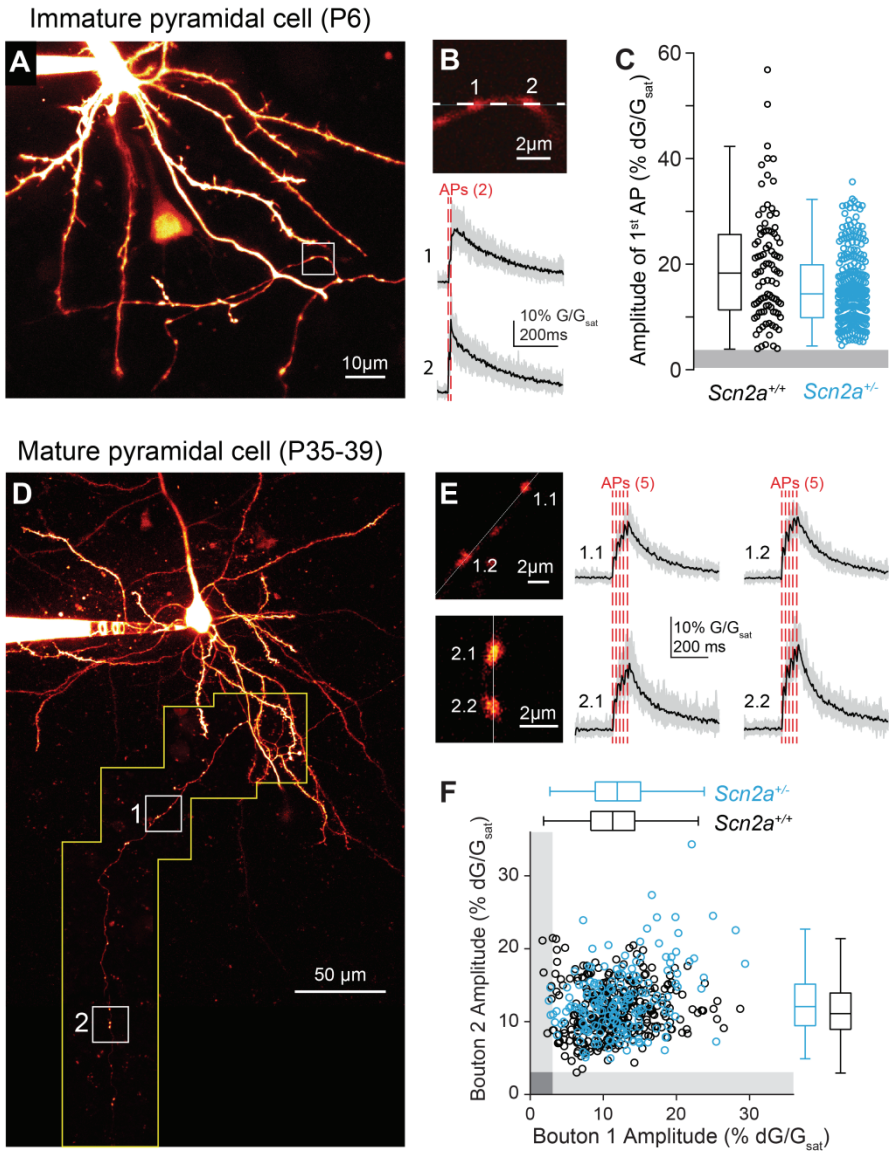

Supplemental Figure 2: APs reliably evoke calcium transients in axonal boutons of *Scn2a*$^{+/-}$ pyramidal cells
(Related to Figures 1, 3)

A: 2PLSM z-stack of basal dendrites and axon of an immature pyramidal cell filled with Alexa-Fluor 594. White box: location of example boutons used for calcium imaging in B.

B: Calcium transients of boutons pairs highlighted in A in response to a train of 2 action potentials at 20Hz. Grey traces are individual sweeps, black are averages of 20 sweeps. Red dotted lines indicate timing of APs.

C: Comparison of calcium transient amplitudes to the first action potential in the train. Failure of the spike-evoked calcium transient to exceed 2 standard deviations above the baseline signal (highlighted by the grey box) was considered an action potential failure. No Failures were observed. 15-20 trials per bouton pairs, 2-4 bouton per cell, 4 cells per genotype.

D: 2PLSM z-stack composite image of basal dendrites and axon of a mature pyramidal cell filled with Alexa-Fluor 594. Yellow bounded area denotes area of higher intensity laser scanning to visualize axons. White boxes: bouton pairs used for calcium imaging in E.

E: Calcium transients of boutons pairs highlighted in D in response to a train of 5 action potentials at 20Hz. Grey traces are individual sweeps, black are averages of 20 sweeps. Red dotted lines indicate timing of APs.

F: Comparison of calcium transient amplitudes of individual sweeps for each bouton pair in response to a single action potential (e.g., the first of the 5 APs shown in B). The coincident failure the spike-evoked calcium transient to exceed 2 standard deviations above the baseline signal (highlighted by the grey box) was considered an action potential failure. No coincident failures were observed. 15-20 trials per bouton pairs, 4-8 bouton pairs per cell, 3-4 cells per genotype.

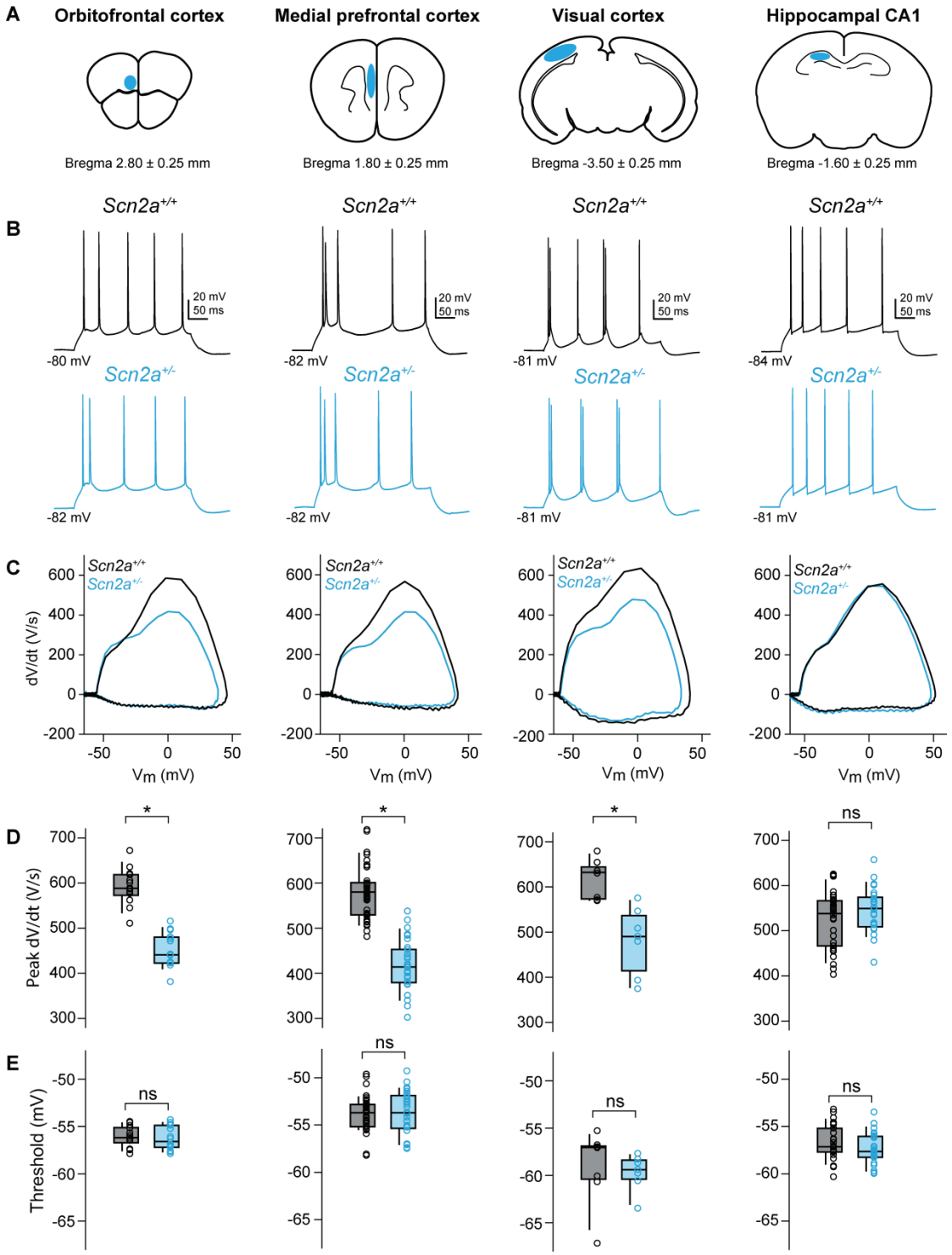

Supplemental Figure 3: Peak action potential speed is reduced in neocortical, but not hippocampal pyramidal neurons
(Related to Figures 1, 3)

A: Schematics of coronal sections indicating recording regions in orbitofrontal cortex, medial prefrontal cortex, visual cortex, and hippocampal CA1.

B: Example spiking generated from *Scn2a*$^{+/+}$ and *Scn2a*$^{+/}$ pyramidal neurons (thick-tuft layer 5 neurons in neocortex) for regions indicated in A.

C: Example phase-plane plots of spike at rheobase from *Scn2a*$^{+/+}$ and *Scn2a*$^{+/}$ pyramidal neurons (thick-tuft layer 5 neurons in neocortex) for regions indicated in A.

D: Comparison of peak rising dVdt. Open circles are single cells. Box plots are median, quartiles, and 90% tails. $p < 0.001$, $F_{genotype}(3,158) = 30.39$, 2-way ANOVA. *: $p < 0.001$, Bonferroni post-hoc test.

E: Comparison of threshold. $p > 0.05$, $F_{genotype}(3,158) = 0.52$, 2-way ANOVA.

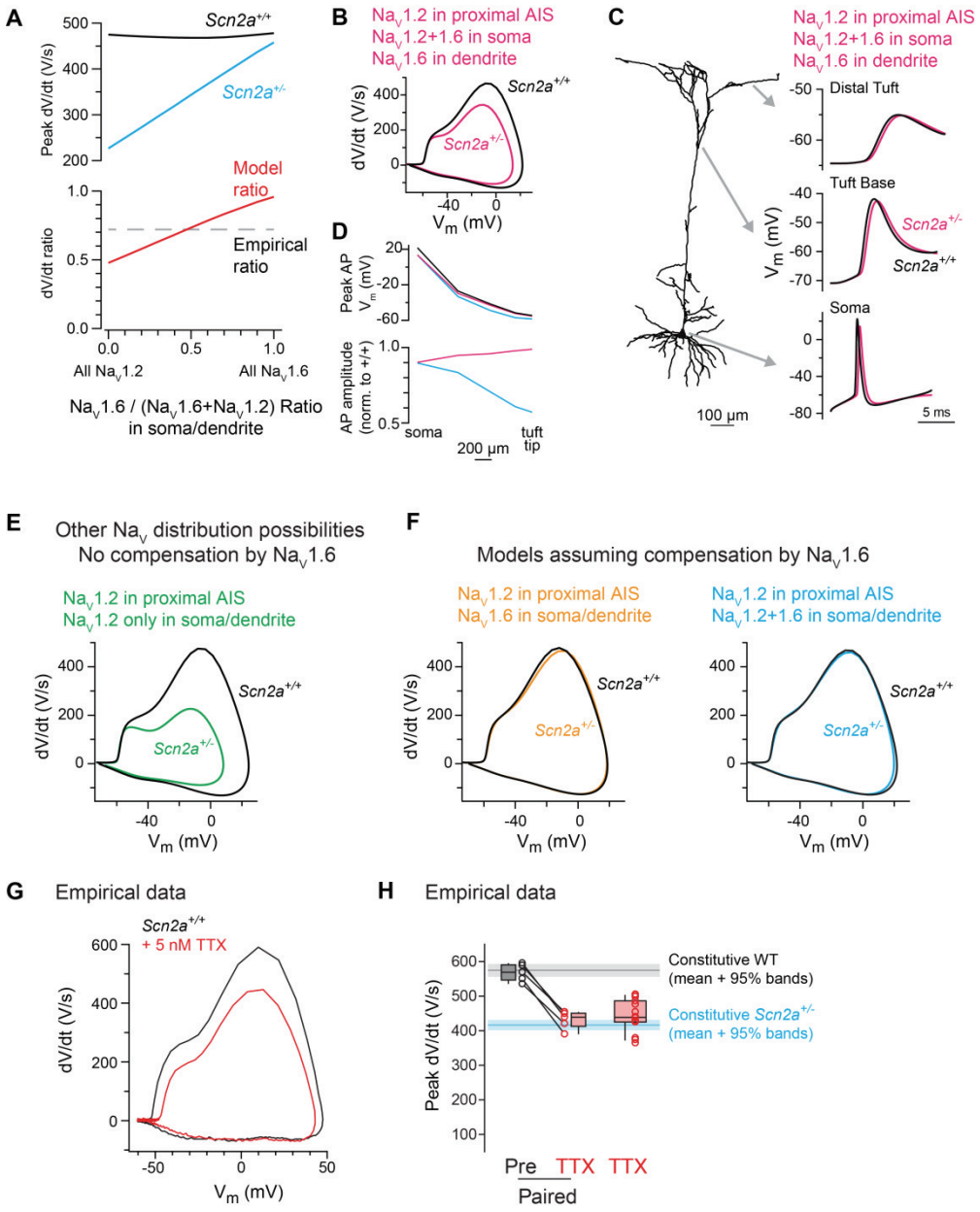

Supplemental Figure 4: Modeling $Na_V1.2$ loss in pyramidal cells with different Na_V compartmental distributions and mimicking *Scn2a*$^{+/-}$ with sub-saturating TTX (Related to Figures 1, 3, 6)

A: Top, the peak rising phase dV/dt in cells expressing different ratios of $Na_V1.2$ vs $Na_V1.6$ in the somatodendritic compartment in WT and *Scn2a*$^{+/-}$ conditions. Bottom, ratio of *Scn2a*$^{+/-}$ to WT peak dV/dt vs. ratio of $Na_V1.2$ vs $Na_V1.6$ in the somatodendritic compartment. Larger relative reductions in peak dV/dt are observed in cases where NaV1.2 dominates the somatodendritic Na_V conductance. The ratio that best matches empirical observations (dashed grey line) occurs when equal numbers of $Na_V1.2$ and $Na_V1.6$ are expressed in the somatodendritic compartment.

B: Compartmental model of cortical layer 5 pyramidal cell where $Na_V1.2$ expression is restricted to the proximal AIS and is co-expressed in equal levels with $Na_V1.6$ in the soma. In this model configuration, $Na_V1.6$ is the only channel isoform in the dendrite. Note that both models resemble empirical observations, suggesting that proximal AIS and somatic $Na_V1.2$ channel distributions largely influence phase plane shape recorded at the soma.

C: Backpropagation of single spikes for conditions modeled in (B). AP waveform is shown at several points along dendritic arbor, including the base of the apical tuft and the distal part of the apical tuft. No major differences are observed in backpropagation when $Na_V1.2$ is only in the AIS and soma (right). Thus, while this model can account for empirically observed differences in somatically recorded dV/dt, it cannot account for deficits in bAP evoked dendritic Ca transients (Fig. 2).

D: Peak voltage for single backpropagating spikes and AP amplitude relative to WT for conditions modeled in Main Figure 2.

E: Left, Model in which $Na_V1.2$ is the only Na_V isoform expressed throughout the somatodendritic compartment. *Scn2a* haploinsufficiency in this condition alters dV/dt far more dramatically than observed experimentally.

F: Models in which $Na_V1.2$ loss in different compartments is compensated by increased expression of $Na_V1.6$. Two cases modeled in Fig. 2 are considered (same color code). Note marginal change to phase plane plot, suggesting that compensation is unlikely in *Scn2a*$^{+/-}$ conditions.

G: Example phase-plane plots of action potential from a cell pre and post treatment with 5nM TTX.

H: Peak action potential velocity for cells pre and post 5nM TTX and cells recorded with 5nM TTX in recording solution at the time of whole-cell recording initiation. Data compared to mean and 95% confidence intervals of *Scn2a*$^{+/+}$ (black/grey) and *Scn2a*$^{+/-}$ (blue) neurons (Fig. 1F).

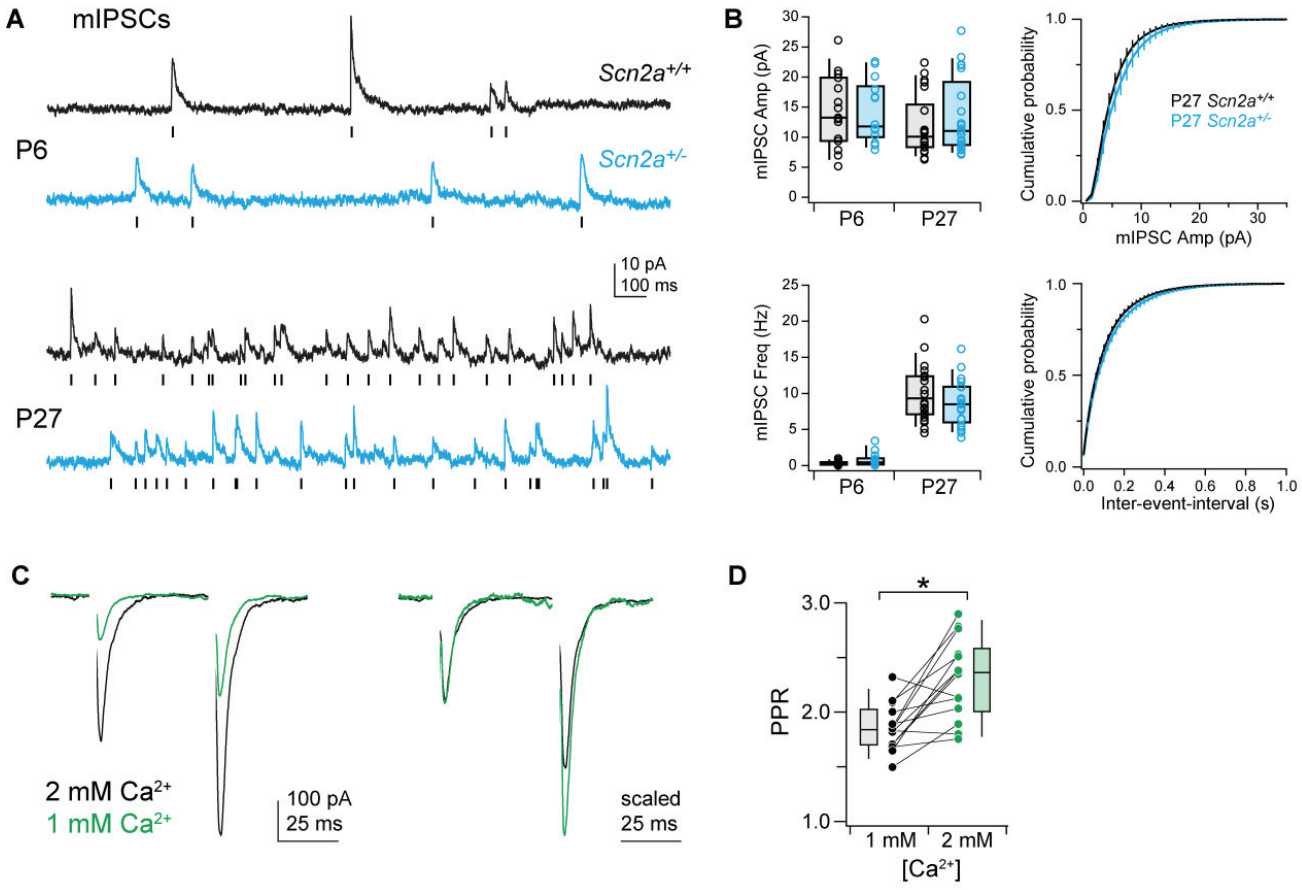

Supplemental Figure 5: mIPSCs and PPR controls.
(Related to Figures 4, 5)

A: Examples of mIPSCs recorded in pyramidal cells voltage-clamped to 0 mV in *Scn2a*$^{+/+}$ (black) and *Scn2a*$^{+/-}$ (cyan) cells. Tick marks denote detected events. Data obtained at P6 (top) and P27 (bottom).

B: Mean mIPSC frequency and amplitude per cell, separated by age. Open circles are single cells. Box plots are median, quartiles, and 90% tails. Cumulative probability histograms were generated per cell, then averaged across all cells. Bars are SEM per data bin. n = 15, 14, 22, 21 for P6 *Scn2a*$^{+/+}$, P6 *Scn2a*$^{+/-}$, P27 *Scn2a*$^{+/+}$, and P27 *Scn2a*$^{+/-}$ cells, respectively. No statistical differences noted.

C: Reducing extracellular calcium from 2 to 1 mM (divalents compensated with $MgCl_2$) in WT neurons reduces EPSC amplitude an increases PPR, demonstrating PPR is sensitive to changes in release probability at these synapses. Left, raw traces. Right, scaled to highlight increase in PPR. Stimulus artifact blanked for clarity.

D: Summary of PPR change evoked by altering extracellular calcium. Circles are single cells. Lines connect data obtained from single cells. Box plots are median, quartiles, and 90% tails. Data obtained at 50 ms ISI only. Asterisk: p = 0.004, Wilcoxon signed rank test, n = 12 cells.

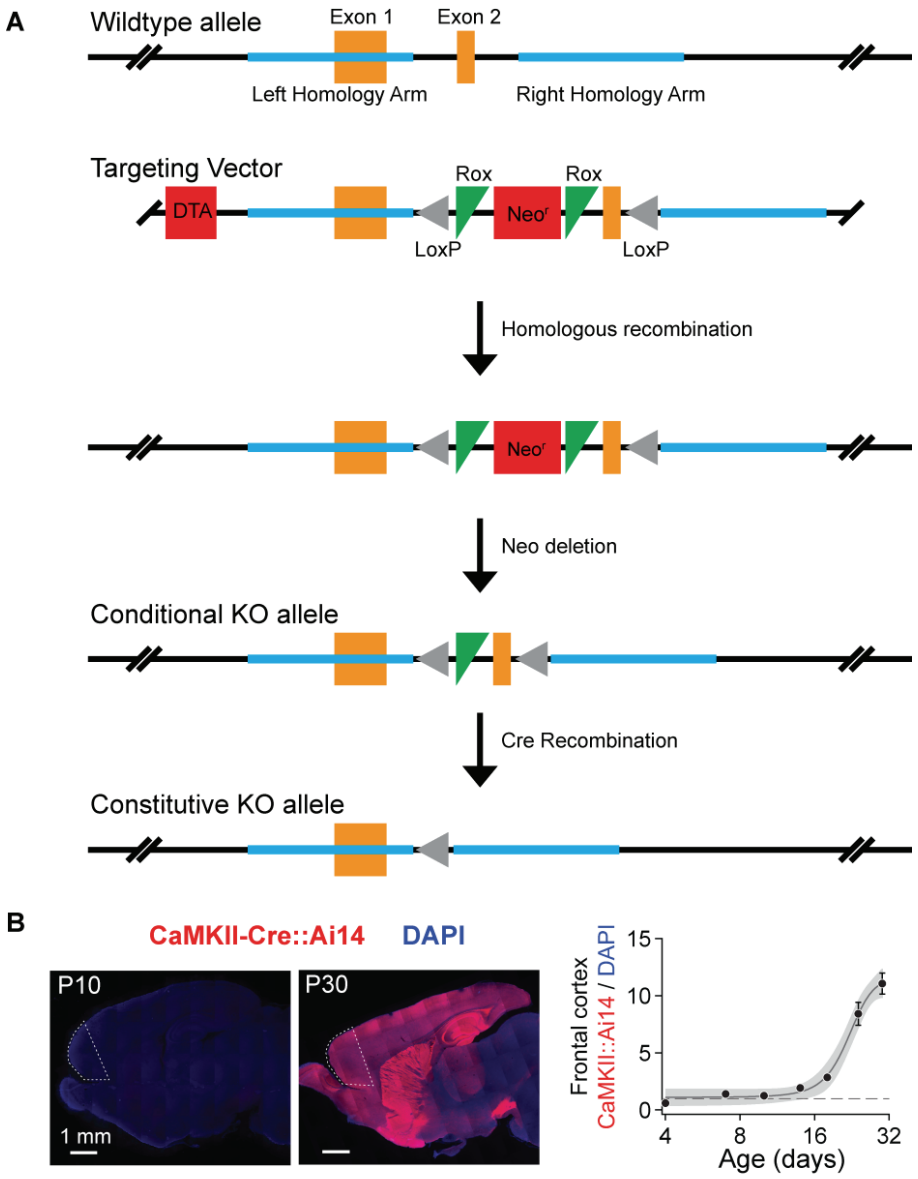

Supplemental Figure 6: Conditional Mouse Construction.
(Related to Figure 6)

A: Schematic overviewing the construction of the conditional *Scn2a*$^{+/fl}$ allele. Briefly, LoxP sites were inserted around exon 2 of the Scn2a gene by homologous recombination in embryonic stem (ES) cells and screened for successful insertion. Positive ES cells were introduced into host embryos and transferred to surrogate mothers, generating F0 chimeras that were outbred with C57BL/6 to generate heterozygous mutants. Please see methods for further details.

B: Left, CaMKII-Cre mice were crossed to Ai14 reporter mice, and tdTomato-mediated fluorescence was measured across development from P4-P32 to determine when Cre-driven tdTomato expression can first be observed in frontal cortex of CaMKII-Cre mice. Values were normalized to DAPI intensity. Measurements were made from frontal cortex regions encapsulated by dashed white perimeter. Right, Ai14/DAPI fluorescence ratio over development, normalized to P4 data. Circles and bars are mean ± SEM at each age (n = 6 sections from 2 animals). Data fit with a generalized logistic function with 95% confidence bands.

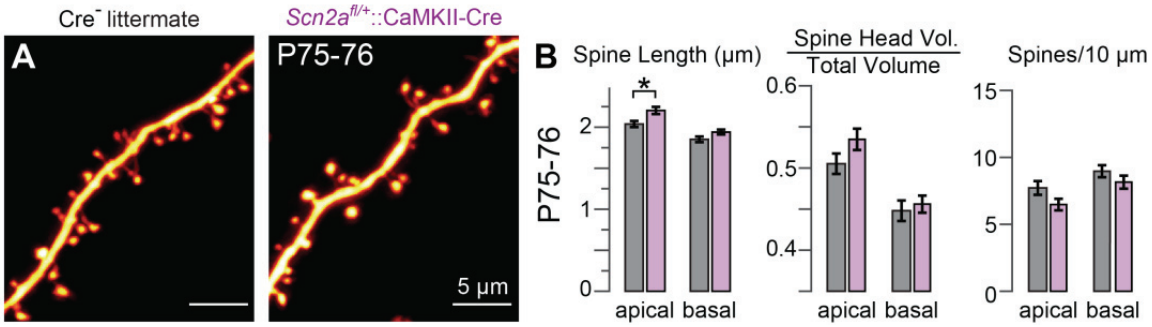

Supplemental Figure 7: Dendritic spines morphology in *Scn2a*$^{fl/+}$::CaMKII-Cre neurons (Related to Figure 5, 6)

A: Examples dendritic spines in p75-76 *Scn2a*$^{fl/+}$::CaMKII-Cre neurons and cre- littermates.

B: Overall spine length from shaft to spine head, volume of spine head relative to total volume of head and shaft, and number of spines per length of dendrite in apical and basal dendrites (n = 588-871 spines per group, 1-3 dendritic branches per cell, 5-6 cells per group). *: $p < 0.05$, Mann-Whitney.

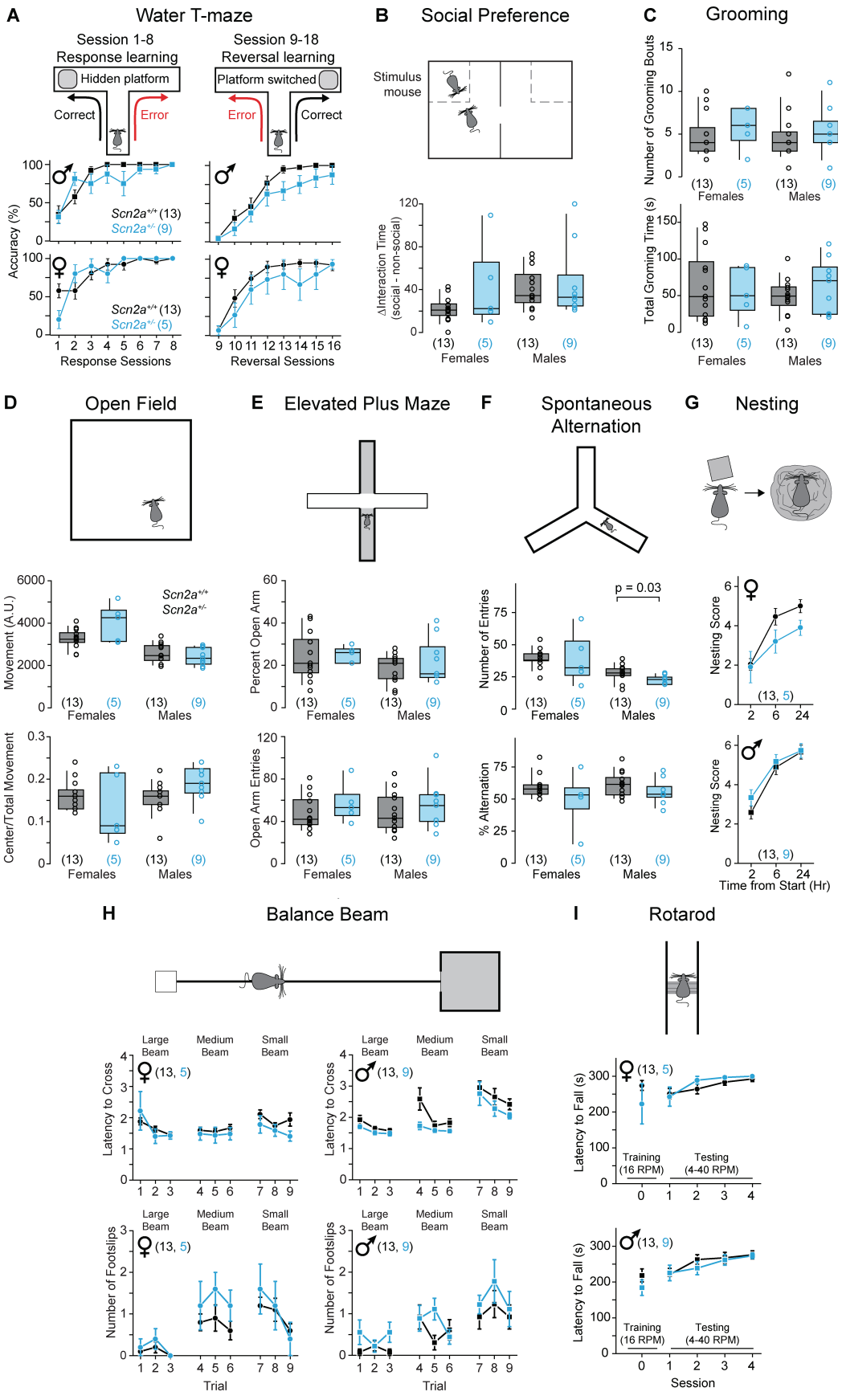

Supplemental Figure 8: Screen of behavioral differences in *Scn2a*$^{+/-}$ mice (Related to Figure 7)

A: Top: schematic of the water T-maze behavioral assay. Mice were placed at the start of a water T-maze and had to identify the arm containing a submerged platform. Accuracy was measured as percentage of trials with correct arm choices. Bottom: Task accuracy for male and female *Scn2a*$^{+/+}$ and *Scn2a*$^{+/-}$ mice across response sessions (2 trials per session) and reversal sessions (3 trials per session). Squares/circles and bars are mean ± SEM.

B: Top: schematic of social preference assay. Mice were placed in a two-chamber container and time spent interacting with a stimulus mouse and an empty cage were recorded. Bottom: Difference in interaction time between social and non-social cages for male and female mice.

C: Screen of grooming behavior differences. Top: number of grooming bouts and bottom: total grooming time of isolated mice over a 10-minute undisturbed period

D: Top: schematic of open field assay to measure locomotor and anxiety-related behaviors. Middle: Screen of grooming behavior differences. bottom: total movement and Right: proportion of movement in the center.

E: Top: schematic of elevated plus maze assay to measure anxiety-related behaviors. Middle: total time spent in the open arms and bottom: total number of open arm entries during an elevated plus maze test.

F: Top: schematic of Y-maze to measure spontaneous alternation. Middle: number of arm entries made and bottom: percent of arm entries contributing to entering all three arms of a Y-maze in succession without repeating an arm (total number of alternations / (total number of entries – 2) *100).

G: Top: schematic of nesting assay. Middle and bottom: nesting scores (methods) of singly housed female and male mice measured at 2, 6, and 24 hours from the start of nest creation.

H: Top: schematic of balance beam assay to measure of motor coordination. Middle and bottom: latency to cross and and number of foot slips while crossing a small, medium or large balance beam (three trials per beam).

I: Top: schematic of rotarod assay to measure of motor coordination. Middle and bottom: latency to fall during rotarod training (16 RPM) and testing (variable speed, 4-40 RPM).

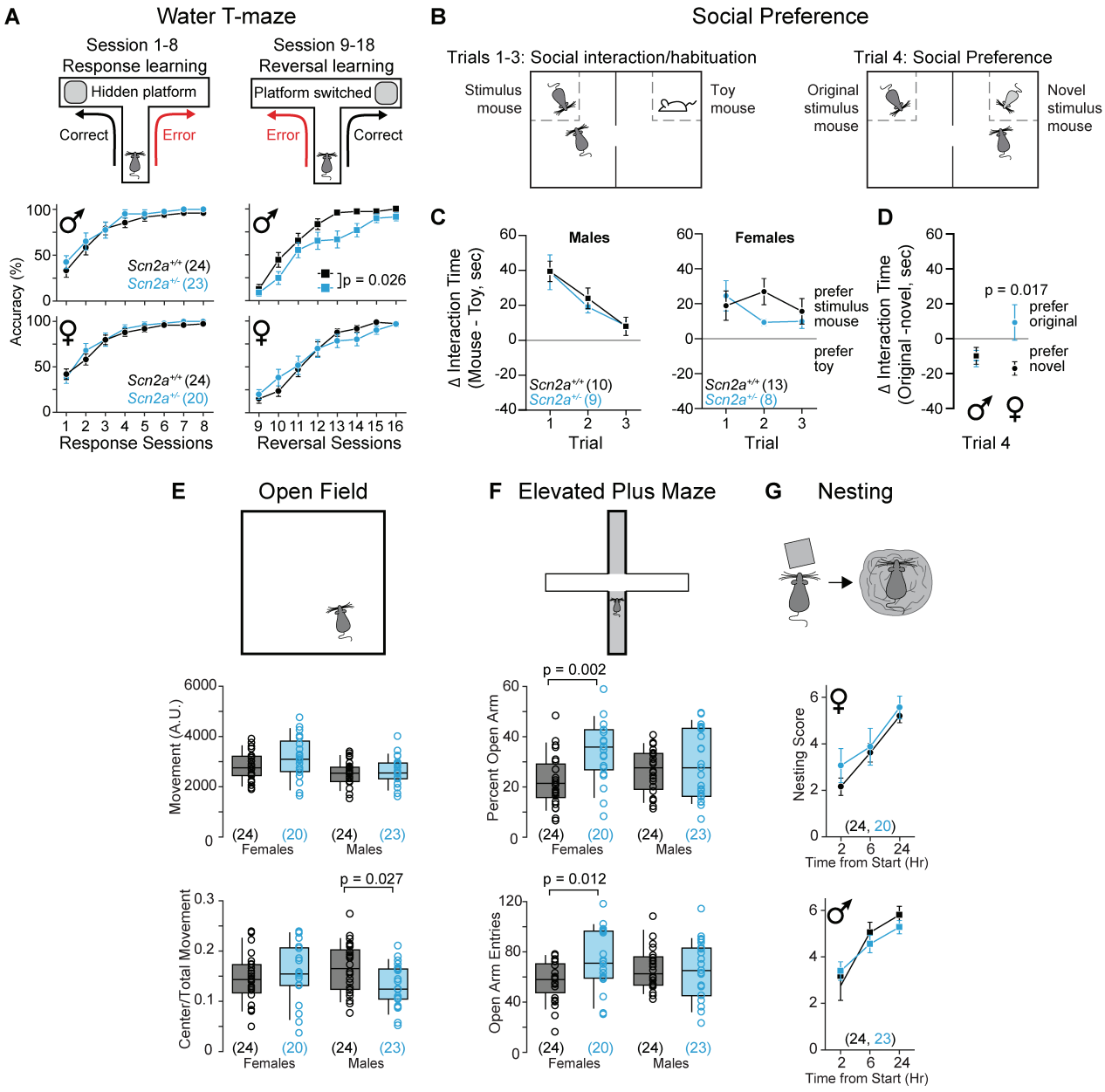

Supplemental Figure 9: Replication of behavioral assays (Related to Figure 7)

A: Top: Schematic of the water T-maze behavioral assay. Mice were placed at the start of a water T-maze and had to identify the arm containing a submerged platform. Accuracy was measured as percentage of trials with correct arm choices. Bottom: Task accuracy for male and female *Scn2a*$^{+/+}$ and *Scn2a*$^{+/-}$ mice across response sessions (2 trials per session) and reversal sessions (3 trials per session). Squares/circles and bars are mean ± SEM. Difference between genotypes, p = 0.026, $F_{Genotype}$ (1, 45) = 5.2, 2-way repeated measures ANOVA.

B: Schematic of social preference assay. Mice were placed in a two-chamber container and time spent interacting with a stimulus mouse (same mouse each trial) and a toy mouse (trials 1-3, social interaction/habituation) or novel stimulus mouse (trial 4, social preference) was recorded.

C: Difference in interaction time of the stimulus mouse and the toy mouse across trials 1-3 for male and female *Scn2a*$^{+/+}$ and *Scn2a*$^{+/-}$ mice. Squares/circles and bars are mean ± SEM. No statistical differences noted.

D: Difference in interaction of the familiar stimulus mouse and a novel stimulus mouse for male and female *Scn2a*$^{+/+}$ and *Scn2a*$^{+/-}$ mice. Squares/circles and bars are mean ± SEM.

E: Top: schematic of open field assay to measure locomotor and anxiety-related behaviors. Middle: Screen of grooming behavior differences. Bottom: total movement and Right: proportion of movement in the center.

F: Top: schematic of elevated plus maze assay to measure anxiety-related behaviors. Middle: total time spent in the open arms. Bottom: total number of open arm entries during an elevated plus maze test.

G: Top: schematic of nesting assay. Middle and bottom: nesting scores (see Methods) of singly housed female and male mice measured at 2, 6, and 24 hours from the start of nest creation.